Including Earth-structure uncertainties in nonlinear moment-tensor estimations

H. Vasyura-Bathke[1,2], J. Dettmer[3], R. Dutta[1], P.M. Mai[1], S. Jónsson[1]

[1] *King Abdullah University of Science and Technology, Thuwal* 23955-6900*, Saudi Arabia*

[2] *Now at: University of Potsdam, D-14476 Potsdam, Germany*

[3] *University of Calgary, Calgary, Canada*

SUMMARY

Earthquake-source parameters can be estimated from seismic waveforms. Since these data indirectly observe the deformation process, parameters of a physical model that quantifies the deformation process are inferred through the inverse problem; which is under-determined. This requires several assumptions to be made about Earth structure and other aspects that affect the source parameter estimation. These assumptions primarily include a simplified seismic velocity model of the Earth waveform and noise models. The specific model choices affect data residuals and can lead to biased source parameter estimations and unrealistic assessment of the associated source-parameter uncertainties. While data errors are routinely included in parameter estimation for full centroid moment tensors, less attention has been paid to theory errors related to velocity model uncertainties and how these affect the resulting moment-tensor uncertainties. Here, we study non-linear full moment

tensors with several simulated data sets and demonstrate that subsurface structure uncertainties can profoundly affect parameter estimation and that their inclusion leads to more realistic parameter uncertainty quantification. We present a solution to include model errors by estimating non-stationary (non-Toeplitz) error covariance matrices that lead to appropriate source-parameter estimates and uncertainties. Finally, we demonstrate the influence of these noise parameterisations on real regional seismic data of the M_l 4.4, 13 June 2015 Fox Creek event, Canada. Including uncertainties in Earth-structure resulted in robust source parameter estimates in case the structure was poorly known.

Key words: Bayesian inference, seismic data, velocity model uncertainties, moment tensor estimation

1 INTRODUCTION

Seismic crustal deformation processes are routinely monitored by broadband seismic networks. Initial source analysis is often based on seismic moment-tensor parameters that assume a point source with fixed location, source-time-function (STF) and simple velocity structure (e.g., Sipkin 1982; Koch 1991; Tocheport et al. 2007). These assumptions can result in erroneous estimates of the parameters of the moment tensor (MT) (Šílen et al. 1992; Kravanja et al. 1999, e.g.). Thus, a more comprehensive approach is to determine the location, the STF and the parameters of the moment tensor simultaneously (e.g., Kravanja et al. 1999; Wéber 2006; Sigloch & Nolet 2006; Ekström 2006; Ekström et al. 2012; Stähler & Sigloch 2014). In addition, these source parameters should be quantified not only in terms of their optimal parameter values, but also in terms of their uncertainties. Uncertainty quantification can be accomplished by formulating the problem via Bayes' Theorem (e.g., Tarantola 2005; Wéber 2006; Dbski 2008; Stähler & Sigloch 2014; Vackář et al. 2017).

The physical processes of earthquake deformation have significant non-linearities in source parameters (Cesca et al. 2016), especially for the origin in space and time, which causes numer-

ical challenges in determining source location and mechanism. In addition, seismic data are contaminated by various noise sources of natural (e.g., meteorological and oceanic) and human origins (Bonnefoy-Claudet et al. 2006). The estimation of noise characteristics is important to obtain appropriate weights for the data in the parameter inference. A simple approach is to estimate the pre-event noise variance and to derive a diagonal weight matrix (e.g., Duputel et al. 2012). To account for data correlations, off-diagonal components of the covariance matrix have been estimated by assuming an exponential decay dependent on the shortest period of the contained frequency-band (e.g., Holland et al. 2005; Duputel et al. 2012). In addition, the covariances between seismogram components can be estimated, these can account for the directionality of seismic noise (Tarantola 2005; Vackář et al. 2017). Accounting for such dependence in noise leads to better estimation of the deformation source parameters and their uncertainties due to a more rigorous quantification of noise.

For inverse problems, it has been shown that both data errors and and errors due to assumptions in the model formulation affect parameter uncertainty (Tarantola & Valette 1982). In source parameter estimation, two significant assumptions are made about the Earth structure (e.g., Tarantola & Valette 1982; Duputel et al. 2014) and the parameterisation of the deformation source (e.g., Dettmer et al. 2014; Pugh et al. 2016). However, errors due to these assumptions have mostly been ignored in source studies (e.g., Hofstetter et al. 2003; Fukuda & Johnson 2008; Baer et al. 2008; Bathke et al. 2013). Recently, there were improvements in incorporating uncertainties in the assumed Earth structure into distributed slip-estimates of extended sources through a prediction covariance matrix. For instance, Yagi & Fukahata (2011) included an additional Gaussian noise term for teleseismic Green's functions and iteratively estimated a prediction covariance matrix in an optimization scheme employing an Akaike's Bayesian information criterion (ABIC). Similarly, Minson et al. (2013) estimated a scale factor for an identity matrix that treats the variance in Green's Functions to account for uncertainty in the subsurface structure in Bayesian inference. With linear perturbations of the original Green's functions, a prediction covariance matrix including off-diagonal terms can be formulated (Duputel et al. 2014). This approach thus includes physical constraints to improve the robustness of finite-fault inversion (Yagi & Fukahata 2008, 2011; Minson et al. 2013; Duputel et al. 2014). Incorporating a prediction covariance matrix to resolve distributed

kinematic rupture parameters for data computed from a synthetic dynamic rupture model, Razafindrakoto & Mai (2014) reported loss in resolution on the kinematic rupture parameters through Bayesian inference by using near-field seismic data. However, they investigated only the effect of the variance in the prediction covariance matrix. In moment tensor estimations the components of the moment tensor can be more robustly estimated by including the location uncertainty of the point source in the inference (Duputel et al. 2012). Hallo & Gallovic (2016) showed that including uncertainties in Earth structure in Bayesian linear moment tensor estimation yields more reliable MT estimates and uncertainties. These developments mostly focused on improving the robustness of determining linearly related source parameters under the premise that the source geometry and location was known (and fixed) *a-priori*. However, it remains unclear if improvements can be achieved when estimating other source parameters that are non-linearly related to the observed waveforms (e. g. source location and geometry) by including uncertainties in Earth structure in the inference.

In this work, we propose a strategy to estimate covariance matrices with respect to uncertainties in Earth velocity models and we show how to include these in Bayesian inference. For simplicity, we approximate the source time function (STF) as a delta function, which is a valid assumption if the source duration is shorter than the shortest periods in the waveforms (Aki & Richards 2002). In synthetic tests we demonstrate the influence of various parameterisations of the covariance matrix on parameter estimates of a full non-linear moment tensor and a non-linear double-couple moment tensor. Finally, we apply the approach to regional seismic data to estimate the source parameters of a full moment tensor for the 13th June 2015, Fox Creek (Canada) event.

2 METHODS

This section provides background information on source parameter estimation with Bayesian inference. In particular, we consider how uncertainties in Earth structure (i.e., layer depths and elastic parameters) are propagated to source parameter uncertainties by estimating theory errors in terms of covariance matrices.

2.1 Bayesian Inference

Bayes' theorem (Bayes 1763) has been widely applied to study earthquake-source processes (e.g., Tarantola & Valette 1982; Wéber 2006; Monelli & Mai 2008; Fukuda & Johnson 2008; Duputel et al. 2012; Minson et al. 2013; Dettmer et al. 2014; Razafindrakoto & Mai 2014; Vackář et al. 2017). Recently, we introduced a flexible software for source estimations in layered elastic halfspaces with Bayesian inference (Vasyura-Bathke et al. 2019, 2020). Using this software, we estimate parameters $\mathbf{m}$ of nonlinear moment tensor parametrizations using seismic data $\mathbf{d}^{obs}$, i.e., seismic displacement waveforms at regional distances.

Assuming Gaussian-distributed noise on the data, a likelihood function is straightforward to formulate. However, since data noise can generally not be determined independently, residual errors $\mathbf{r}(\mathbf{m}) = \mathbf{d}^{obs} - \mathbf{d}(\mathbf{m})$ serve as a proxy. The posterior probability density (PPD) for residual errors of K datasets is given by (Tarantola & Valette 1982)

$$p(\mathbf{m}|\mathbf{d}_{obs}) = c \times p(\mathbf{m}) \times \prod_{k=1}^{K} \frac{1}{(2\pi)^{N/2}|\mathbf{C}_k|^{1/2}} \exp\left[-\frac{1}{2}[\mathbf{d}_k^{obs} - \mathbf{d}_k(\mathbf{m})]^T \mathbf{C}_k^{-1} [\mathbf{d}_k^{obs} - \mathbf{d}_k(\mathbf{m})]\right], \quad (1)$$

where $\mathbf{d}_k(\mathbf{m})$ represent predicted seismic data at seismic station k with N samples that depend on the moment-tensor parameters $\mathbf{m}$, and c is a normalizing constant that is not required here. The covariance matrices $\mathbf{C}_k$ represent the noise statistics, and play an important role in the parameter estimation as well as in the uncertainty quantification.

2.2 Residual error covariance matrix

The residual covariance matrices include variances and covariances of the data residuals $\mathbf{r}_k$. Under the assumption that noise between stations is not correlated, one matrix is required for each station. The total covariance matrix $\mathbf{C}_k$ at station k is the sum of the data covariance matrix $\mathbf{C}_k^d$ that quantifies measurement errors and the model prediction covariance matrix $\mathbf{C}_k^t$ caused by physical and mathematical approximations in the forward model (theory errors),

$$\mathbf{C}_k = \mathbf{C}_k^d + \mathbf{C}_k^t. \quad (2)$$

Many moment-tensor studies ignore off-diagnonal terms in $\mathbf{C}_k^d$ as well as the component $\mathbf{C}_k^t$ (e.g., Cesca et al. 2017; Ekström 2006; Ekström et al. 2012; Vackář et al. 2017). Then, only measurement errors are considered and assumed to be from a stationary, uncorrelated random Gaussian process (Fig. 1a). For long-period data, it can be useful to estimate diagonal (Toeplitz) covariance matrices (Fig. 1b) with exponential decay depending on the shortest period t_0 of the data (Duputel et al. 2012, see Tab. 1). For both types of covariance matrices, variances σ^2 can be estimated from the recorded signal prior to the first arriving wave of the seismic event of interest at any given station. However, it must be ensured that there is no source of seismic signal other than background noise present in the estimation data; otherwise the variance estimation could be biased.

Theory errors due to physical model assumptions made when formulating the geophysical inverse problem can also result in source parameter uncertainties that are substantially larger than those due to measurement errors (Tarantola & Valette 1982). A significant source of theory error is from the source parameterisation. One example of theory error could be a predefined earthquake hypocentre location for focal-mechanism estimation, but this location is inconsistent with the centroid moment-tensor location (Duputel et al. 2012; Ragon et al. 2018). Another example is if the STF is assumed to be of particular shape (e.g., triangular) that is not sufficiently general to describe the moment release of the source (Stähler & Sigloch 2014). Often it is possible to account for such issues by formulating model prediction covariance matrices, but this is beyond the scope of this study.

Yet another important source of theory error is the representation of Earth structure (Minson et al. 2013). While actual subsurface structure is 3D, anisotropic and heterogeneous, Earth structure is most often approximated by an isotropic, horizontally stratified half-space. Here, we build on a previously proposed strategy (Tarantola & Valette 1982; Yagi & Fukahata 2011; Duputel et al. 2014) to include theory error due to Earth-structure assumptions via the model prediction covariance matrix $\mathbf{C}_k^t$. We assume a horizontally stratified, elastic, isotropic half-space with uncertainties in the velocity-depth profile. One approach to estimate $\mathbf{C}_k^t$ in this case is to perturb the Green's Functions that relate changes in velocity profile linearly to the displacements at the Earth's surface (Du et al. 1994; Duputel et al. 2014). Therefore, we calculate the Green's functions for various velocity models, based on the global reference

model AK135 (Kennett et al. 1995) in combination with CRUST2.0 (Bassin et al. 2000) for the crustal structure. Layer velocities and depths are varied in the crust by Gaussian perturbations with 10% standard deviation around the reference model (Mooney 1989) to generate an ensemble of Earth structures. From this ensemble, N_e sets of Green's functions are computed and efficiently stored (Heimann et al. 2019). Let i and j be indices for the rows and columns of the covariance matrix. Then, term $\bar{\mathbf{d}}_{k,i} = \frac{1}{N_e} \sum_{n=1}^{N_e} \mathbf{d}^n_{k,i}(\mathbf{m})$ is the sample mean over N_e predicted data vectors at station k (a similar term is defined for j) and a covariance matrix $\mathbf{C}^t_k$ is computed according to (Duputel et al. 2012)

$$\mathbf{C}^t_{k,ij}(\mathbf{m}) = \frac{1}{N_e} \sum_{n=1}^{N_e} (\mathbf{d}^n_{k,i}(\mathbf{m}) - \bar{\mathbf{d}}_{k,i})(\mathbf{d}^n_{k,j}(\mathbf{m}) - \bar{\mathbf{d}}_{k,j}). \tag{3}$$

This model-prediction covariance matrix needs to be computed with respect to source parameters $\mathbf{m}$ while predicted data $\mathbf{d}^n_k$ are computed for each realization of Earth structure n (sets of Green's functions) and for each seismic station k. This covariance matrix $\mathbf{C}^t_k$ can be included in the likelihood function for inference following eqns. 1 and 2. Such formulation implies computing the synthetic seismic waveforms for each variation in the Earth structure (Fig. 2). As it is prohibitively expensive to calculate a realization of $\mathbf{C}^t_k$ in each iteration of a Monte Carlo algorithm, we assume that $\mathbf{C}^t_k$ changes less rapidly than the source parameters $\mathbf{m}$ in the sampling algorithm and we update it only periodically (Duputel et al. 2014). This approach accounts for errors in subsurface structure in addition to data errors in the estimation of source-parameters and their uncertainties. Figure 1 (c & d) demonstrates that theory errors due to Earth structure result in non-stationary covariance matrices with time-dependent error statistics.

Such calculation of $\mathbf{C}^t_k$ is computationally very expensive and depends on the assumed variability of the Earth structure. If this variability is poorly known, the approach may result in over- or underestimated parameter uncertainties. An alternative approach is to estimate non-stationary/non-Toeplitz covariance matrices $\mathbf{C}$ (Fig, 1e)) based on data residuals (Dettmer et al. 2007). This approach naturally includes both data and theory errors, is fast and non-parametric, but has the limitation of depending on an initial assumption of uncorrelated errors. The non-stationary/non-Toeplitz matrix depends on the forward model and can be

computed from parameters estimated initially assuming uncorrelated stationary errors. Here, we do not rely on that initial assumption. However, some problems may exhibit convergence issues when this assumption is not relied on.

In the following we use the terms: *variance*, *exponential*, *variance_cov*, *exponential_cov* and *non-Toeplitz* to distinguish between the different covariance parameterisations described above and listed in Tab. 1.

3 SIMULATION RESULTS

3.1 Simulated Data

To demonstrate the effect of the covariance matrix parameterisation and the influence of including velocity model uncertainties in earthquake source-parameter estimations, we present two simulated test cases. We generate two sets of simulated seismic displacement waveforms based on two different Earth structures (Tab. 2, Fig. 2a, blue and red lines) for a double-couple moment-tensor source (Tab. 3). We refer to these Earth structures as *reference structures* in the following. For each test case we estimate the source parameters of a full moment tensor using the simulated data with the five different covariance matrix parametrizations (Tab. 1, Sec. 2.2).

In these test cases, we simulate theory errors due to unknown Earth structure by assuming a different Earth structure for the source estimations than that of the reference model. We refer to this modified structure as the *estimation structure*. If no local Earth model is available in the study region, one would typically use some global model for the estimation. Here, we employ the global AK135 velocity model (Kennett et al. 1995) in combination with CRUST2 (Bassin et al. 2000) (Fig. 2a)) as the estimation structure for each test case. In the first test case, case 1, the reference structure has the same number of layers as the estimation structure, but layer velocities and depths differ $< 10\%$ (Tab. 2, Fig. 2a). In the second case, case 2, the reference structure (Hofstetter et al. 2003) differs significantly from the estimation structure with a different number of layers, layer velocities and depths (Fig. 2a).

We created the reference synthetic kinematic displacements for both test cases with frequencies up to 2 Hz for ten seismic stations at regional epicentral distances (up to 1000 km)

(Tab. 3, Fig. 3). We added uncorrelated, Gaussian-distributed noise with a variance of 5% of the maximum waveform amplitude for each station. We filtered the data between 0.01 and 0.1 Hz and rotated waveform components to transverse and vertical directions to estimate the moment-tensor parameters and its centroid location. For each test case, we estimated marginal distributions of source parameters while only changing the noise parameterisation (Fig. 1, Tab. 1), to demonstrate the influence of $\mathbf{C}$ on the results. Following the procedure in Sec. 2.2, the estimation structure was randomly perturbed 20 times to estimate $\mathbf{C}_k^t$ in the course of the sampling.

3.2 Results

For case 1 (small theory errors), estimation results are summarized in Fig. 4 in terms of posterior marginal probability densities. A notable observation is that when only applying $\mathbf{C}_k^d$ (i.e., ignoring theory error), the ranges of values obtained by the estimation do not include true parameter values. This result shows a significant limitation of applying only measurement errors in the estimation. In particular, the *exponential* noise parameterisation performs poorly and only the centroid location shows reasonable estimates. The variance parameterisation performs better, but marginals of the location parameters exhibit significant bias, while some moment-tensor components are resolved (e.g., m_{ee}, m_{ne}).

Including the $\mathbf{C}_k^t$ term leads to increased width of the posterior marginals, but more importantly, both noise parameterisation types (*variance_cov* and *exponential_cov*) resolve all moment-tensor parameters (Fig. ,4). However, the location marginals are significantly wider than observed for other noise parameterisations. In addition, the true value of north-shift is not recovered when using *variance_cov*. The *non-Toeplitz* parameterisation also resolves the parameters, although in some instances, true parameter values are in the tail of the marginals (e.g., north-shift, m_{nd}, m_{ed}). The centroid time is poorly recovered by all other noise parameterisations.

The results for case 2 (large theory errors) are summarized in Fig. 5. Here, it is clear that only using $\mathbf{C}_k^d$ causes significant errors and true parameter values are rarely recovered (*variance* and *exponential* results in Fig. 5). The marginals exhibit even stronger biases with respect to the true values. While the location parameters (east-shift, north-shift and depth)

are recovered by the *exponential* parameterisation in case 1, these are biased here. The moment tensor components are not recovered in either case.

Including $\mathbf{C}_k^t$ has the noticeable effect of substantially widening marginals (*exponential_cov* and *variance_cov* results in Fig. 5), like for case 1. Only some of the marginals include the true value for these parameterisations (e.g., m_{nn}, m_{ee}), while many marginals are biased and the true values are not recovered. In contrast, the *non-Toeplitz* parameterisation recovers true values appropriately and with low uncertainty for most parameters. The centroid time is poorly recovered for all parametrizations, but magnitude is well recovered with all parameterisations, except for the *variance*, which underestimates.

3.3 Residual Analysis

To increase confidence in the estimation results, we analyze the statistics of the data residuals. Since we assume Gaussian-distributed residuals with some covariance matrix (eq. 1), both Gaussianity and randomness of standardized residuals should be tested. Standardized residuals are obtained by scaling raw residuals with their covariance matrix. That is to say, $\hat{\mathbf{r}_k} = \mathbf{L}_k^{-1}\mathbf{r}_k$, where $\mathbf{L}_k$ is the lower triangle of the Cholesky decomposition of the total covariance matrix $\mathbf{C}_k = \mathbf{L}_k\mathbf{L}_k^T$. If the covariance matrix applied in the estimation agrees well with the actual correlations, the standardized residuals are uncorrelated Gaussian distributed with unit variance. That is to say, standardized residuals should be from an uncorrelated random process, which can be assessed by considering their auto-correlations and histograms. Ideally, the auto-correlation functions should exhibit a sharp central peak and no or small sidelobes. Histrograms should agree closely with a Gaussian PDF with unit variance (Dettmer et al. 2008).

Histograms of standardized residuals for cases 1 and 2 (Fig 6, station-individual histograms Supplemental Figs. S6-S10) show that for the parameterisations of *variance* and *exponential* the assumption of Gaussianity of residuals is not met in the estimation. These distributions are more heavily tailed and peaked than Gaussian distributions. Including, $\mathbf{C}_k^t$ vastly improves this issue and the standardized residuals are more Gaussian. In particular, peak height is reduced (i.e., reduced overfitting of data). However, the distributions exhibit extensive tails with large standard deviations. The *variance_cov* performed better than the *exponential_cov* in this

case, while the *non-Toeplitz* parameterisation shows standardized residuals with satisfactory Gaussianity.

The station-individual autocorrelations show that parametrizations *variance* and *exponential* have long-wavelength sidelobes (Supplemental Figs. S1, S3). This means that residuals contain significant residual correlations that the covariance model in the estimation could not capture. Including $\mathbf{C}_k^t$ reduces the residual correlation for both parametrizations (Supplemental Figs. S2, S4). The *non-Toeplitz* covariance accounts for most correlations and standardized residuals appear close to random white noise (Supplemental Fig. S5). This result suggests that *non-Toeplitz* covariance matrices produce results that are most consistent with the assumptions made in the estimation and can successfully address problems with significant theory error.

3.4 Moment tensor decompositions

To evaluate the focal-mechanism representation of the sampled moment-tensor components, moment-tensors can be decomposed into isotropic and deviatoric components (Jost & Hermann 1989). The deviatoric component can be split further into the compensated linear vector dipole (CLVD) and double-couple (DC) components. We applied such a decomposition to the moment tensor components of the PPDs of both setup cases for each noise parameterisation. In general, the different percentages of the MT components vary between different noise parameterisations.

For case 1, the differences are noticeable, e.g., *variance* and *exponential* show isotropic components between ∼5 and ∼10 percent, respectively. Significant CLVD components of up to ∼20 and ∼25 percent were estimated by using the *exponential* and *exponential_cov* noise parameterisations, respectively (Fig. 7a). For case 2 , *exponential* and *exponential_cov* show noticable isotropic components, while the CLVD component of the *variance_cov*, *exponential* and *exponential_cov* noise parameterisations is significant (Fig. 7b).

Since the target source was a pure double-couple moment tensor, it is obvious that theory errors cause significant, erroneous CLVD and isotropic MT components if the noise parameterisation of the covariance matrix is inappropriate. In this regard, the *non-Toeplitz* noise parameterisation outperformed all the other parameterisations with overall the smallest errors

in estimating isotropic and CLVD components for both cases. However, it is worth noting that the *variance* noise parameterisation is the second best.

3.5 Double-Couple Moment Tensors

Sometimes, moment tensors are estimated under the assumption of a pure double-couple model for the earthquake. This assumption removes the possibility estimating erroneous isotropic or the CLVD components. Consequently, the estimation may be more successful as long as this assumption is consistent with the actual rupture mechanism. Figure 8 presents results (Tab. 2) for assuming a pure double-couple moment tensor model. For case 1, *variance* and *exponential* parameterisations cannot recover the true values (Fig. 8). Including $\mathbf{C}_k^t$ allows to recover true parameters, but neither location nor time parameters are estimated well. While parameters are not fully recovered by the *exponential* parameterisation, there is a vast improvement when including $\mathbf{C}_k^t$ (e.g., rake, time, depth, magnitude). Only the *non-Toeplitz* parameterisation recovered the true source mechanism, magnitude and centroid location. The centroid time was recovered only by the *exponential_cov* noise parameterisation.

For large theory errors the source mechanism and location could only be recovered by the *non-Toeplitz* parametrization (Fig. 9). Including $\mathbf{C}_k^t$ did not help to reliably recover the true parameter values. Only the source magnitude was recovered by most parameterisations, except for the *variance* parametrization.

Our results show that under the assumption of a double-couple moment tensor, source parameters can be biased if correlated, non-stationary data errors are ignored in the noise parameterisation of the covariance matrix. Similar to the results for the full moment tensor, for small theory errors, including $\mathbf{C}_k^t$ improved source parameter estimates. For large theory errors, only the *non-Toeplitz* parameterisation resolved the true source parameters successfully.

4 APPLICATION TO FOX CREEK EARTHQUAKE

This section applies the various approaches to theory-error estimation to a regional earthquake. Regional seismic data are considered for the M_l=4.4 earthquake on 13 June 2015 near

Fox Creek, Alberta, Canada (Wang et al. 2016) (Fig. 10). The event is related to hydraulic fracturing operations in this area, which was previously seismically relatively inactive (Schultz et al. 2015). Thus, the possibility of sizable non-couple source components due to fluid effects could be expected, and hence it is justified to do a full moment tensor estimation.

We use data from stations up to a distance of 300 km wrt. the event location from the gCMT catalog at latitude 54.102° and longitude -116.95°. We convert the data to displacement waveforms, downsample them to 1.0 Hz and rotate them to radial (R), transverse (T) and vertical (Z) components. We then estimate parameters (location, MT components, centroid time) of a full moment tensor using body waves (band-pass filtered to 0.08-0.3Hz) and surface waves (band-pass filtered to 0.04-0.1Hz) for each noise parameterisation (Tab. 2).

To test our method we use two reference subsurface structures, a regional structure (Wang et al. 2016) and the global AK135 earth structure (Kennett et al. 1995) (Supplemental material Fig. S11). Following our procedure from Sec. 2.2, we vary these reference structures 20 times each with standard deviations of 15% and 35% for velocity and layer depth values for the regional structure and 15% and 10% for the global structure (Supplemental material Fig. S11).

4.1 Results

For the regional subsurface structure, estimation results are summarized in Fig. 11 in terms of marginal probability densities. It is most striking that *variance*, *exponential* and *non-Toeplitz* parameterisation show similar results all across parameters. This observation implies that it is not necessary to account for non-stationary correlated noise and that the theory error is small. Including $\mathbf{C}_k^t$ into estimation significantly widens the marginals and results in shifts of the marginals (e.g. magnitude, depth, m_{ne}). By artificially introducing theory error through $\mathbf{C}_k^t$ the *variance_cov* and *exponential_cov* marginals resemble uncertainty, which in reality may not be present, correspondingly we likely overestimated the errors in the regional structure (supplementary material Fig. S11a). Consequently, the results become worse accounting for theory error in this case when the subsurface structure seemed to be well known.

For the global subsurface structure, estimation results of *variance* and *exponential* parameterisations show higher magnitude estimates and earlier centroid times as well as shallower

source depth (Fig. 12). Results become more consistent including $\mathbf{C}_k^t$ and *variance_cov* and *exponential_cov* marginals mostly contain the *non-Toeplitz* marginals. The *exponential_cov* and *variance_cov* parameterisations lose the source depth resolution. This indicates that the global structure contains significant theory error for data of the study area and accounting for it through $\mathbf{C}_k^t$ helped in this case.

We note that the published solution of Wang et al. (2016) is contained in the marginals of *variance*, *exponential* and *non-Toeplitz* by using the regional structure and it is contained in the somewhat wider marginals for *variance_cov*, *exponential_cov* and *non-Toeplitz* by using the global structure.

The fit to the data is in this case better for the surface wave arrivals than for the body wave arrivals due to the lower frequency content (Fig. 13). Including $\mathbf{C}_k^t$ mostly leads to larger variations in amplitude of predicted waveforms for body wave arrivals (supplemental material Fig. S12). Not surprisingly the fit to the data is better when using the regional subsurface structure rather than the global subsurface structure (supplemental material Fig. S13).

To better visualize and interpret the marginals of the sampled moment tensor components we apply moment tensor decomposition (also see Sec. 3.4) for each noise parameterisation and subsurface structure (Fig. 14). It is noticable that in case of a poor choice of noise parameterisation the isotropic component seems to be large, i.e. *variance_cov* and *exponential_cov* for the regional structure and *variance* and *exponential* for the global structure.

Wang et al. (2016) report a CLVD component of $\sim 23 \pm 17\%$ which is lower and more uncertain than our estimates obtained using the regional subsurface structure. Using the global structure the CLVD component is poorly constrained. If the event was indeed caused by hydraulic fracturing a large CLVD component would not be unlikely.

5 DISCUSSION AND CONCLUSION

We investigated the influence of noise parameterisation on the estimated parameters of a non-linear full moment-tensor in a layered elastic half-space by means of Bayesian inference using synthetic and real seismic data at regional distances. Five different ways of covariance estimation were tested in the presence of small and large theory errors caused by assuming a

wrong velocity structure of the Earth. Repeated perturbation of the Earth structure model and subsequent forward simulation of the seismic waveforms allows to estimate a prediction covariance matrix $\mathbf{C}_k^t$ describing the theory error.

Including $\mathbf{C}_k^t$ in the estimation improves parameter estimates if the velocity-model variations that are used for computing $\mathbf{C}_k^t$ cover the true velocity model (case 1 and Fox Creek global). If the true velocity model is not covered by the variations of the velocity models, including $\mathbf{C}_k^t$ into the optimization does not lead to better parameter estimates (case 2). Parameter uncertainties also depend on the chosen distribution for velocity and layer depth errors employed to compute $\mathbf{C}_k^t$. Notably, this likely is a subjective choice with limited information available to aid this process. Depending on the choice of velocity errors, uncertainties will likely be larger than for other parameterisations and may be even biased (Fox Creek regional).

Estimating $\mathbf{C}_k^t$ with the approach chosen here is computationally expensive as the variations in Earth structure require generating the Green's Functions for many velocity profiles. To improve the efficiency of computing $\mathbf{C}_k^t$, Hallo & Gallovic (2016) developed an approach that could allow to update $\mathbf{C}_k^t$ in every step of the sampling. The method was applied to moment tensors assuming known centroid location. However, matrix inversion/decomposition is still required and may be computationally costly. Similar to the approach presented here their approach also requires calculation of Green's Functions for a distribution of velocity profiles which may be difficult to constrain objectively.

Errors in Earth structure may lead to correlated data error since data are band limited and sampled discretely in space and time (Stähler & Sigloch 2016; Hallo & Gallovic 2016). To account for spatially correlated data errors across stations, Stähler & Sigloch (2016) employed an empirical likelihood function based on a waveform cross-correlation criterion. Our likelihood function is rigorous in that it is formally derived from the assumption of Gaussian-distributed residuals but ignores spatial correlations between stations.

In conclusion, our results suggest that applying the *non-Toeplitz* covariance matrix parameterisation provides a reliable and, straightforward approach to account for correlated errors in source parameter estimation. The results produced with this parametrization performed best in the test cases considered in this work. The formulation is non-parametric and therefore

fast to compute. Importantly, it intrinsically accounts for all theory errors, including but not limited to errors due to Earth-structure mismatch and centroid location mismatch.

The noise parameterisations presented here are implemented in the open software BEAT (Vasyura-Bathke et al. 2019, 2020). Users are free to apply BEAT without the need for additional implementation. BEAT also provides the opportunity to apply these noise parametrizations to rectangular sources and finite fault models.

6 ACKNOWLEDGMENTS

We thank Mehdi Nikkhoo, Frank Krüger and Olaf Zielke for valuable discussions. Plots were produced by using *Matplotlib* and Generic Mapping Tools (Hunter 2007; Wessel et al. 2013). This work has been implemented using the open source library *pyrocko* (Heimann et al. 2017). This research was supported by King Abdullah University of Science and Technology (KAUST), under award numbers BAS/1/1353-01-01 and BAS/1/1339-01-1. H.V-B was partially supported by Geo.X, the Research Network for Geosciences in Berlin and Potsdam under the project number SO_087_GeoX.

REFERENCES

Aki, K. & Richards, P. G., 2002. *Quantitative seismology*, University Science Books, 2nd edn.

Baer, G., Funning, G. J., Shamir, G., & Wright, T. J., 2008. The 1995 November 22, M w 7.2 Gulf of Elat earthquake cycle revisited, *Geophys, J. Int.*, **175**(3), 1040–1054.

Bassin, C., Laske, G., & Masters, G., 2000. The current limits of resolution for surface wave tomography in North America, *EOS Trans. AGU*, **81**(F897).

Bathke, H., Sudhaus, H., Holohan, E., Walter, T. R., & Shirzaei, M., 2013. An active ring fault detected at Tendürek volcano by using InSAR, *J. Geophys. Res. Solid Earth*, **118**(8), 4488–4502.

Bayes, T., 1763. An Essay towards Solving a Problem in the Doctrine of Chances, *Phil. Trans.*, **53**, 370–418.

Bonnefoy-Claudet, S., Cotton, F., & Bard, P. Y., 2006. The nature of noise wavefield and its applications for site effects studies. A literature review, *Earth Sci. Rev.*, **79**(3-4), 205–227.

Cesca, S., Grigoli, F., Heimann, S., Dahm, T., Kriegerowski, M., Sobiesiak, M., Tassara, C., Olcay, M.,

Potsdam, G., Potsdam, D., & E-mail, G., 2016. The Mw 8.1 2014 Iquique, Chile, seismic sequence: a tale of foreshocks and aftershocks, *Geophys, J. Int.*, **204**, 1766–1780.

Cesca, S., Heimann, S., Kriegerowski, M., Saul, J., & Dahm, T., 2017. Moment Tensor Inversion for Nuclear Explosions : What Can We Learn from the 6 January and 9 September 2016 Nuclear Tests , North Korea ?, *Seismol. Res. Lett.*, **88**(2A).

Ching, J. & Chen, Y.-C., 2007. Transitional Markov Chain Monte Carlo method for Bayesian model updating, model class selection, and model averaging, *J. Eng. Mech.*, **133**(7), 816–832.

Dettmer, J., Dosso, S. E., & Holland, C. W., 2007. Uncertainty estimation in seismo-acoustic reflection travel time inversion, *J. Acoust. Soc. Am.*, **122**(1), 161–176.

Dettmer, J., Benavente, R., Cummins, P. R., & Sambridge, M., 2014. Trans-dimensional finite-fault inversion, *Geophys, J. Int.*, **199**(2), 735–751.

Du, Y., Segall, P., & Gao, H., 1994. Dislocations in inhomogeneous media via a moduli perturbation approach : General formulation and two-dimensional solutions, *J. Geophys. Res.*, **99**, 13767–13779.

Duputel, Z., Rivera, L., Fukahata, Y., & Kanamori, H., 2012. Uncertainty estimations for seismic source inversions, *Geophys, J. Int.*, **190**(2), 1243–1256.

Duputel, Z., Agram, P. S., Simons, M., Minson, S. E., & Beck, J. L., 2014. Accounting for prediction uncertainty when inferring subsurface fault slip, *Geophys, J. Int.*, **197**(1), 464–482.

Dbski, W., 2008. Estimating the earthquake source time function by Markov Chain Monte Carlo sampling, *Pure appl. geophys.*, **165**(7), 1263–1287.

Ekström, G., 2006. Global detection and location of seismic sources by using surface waves, *Bull. Seismol. Soc. Am.*, **96**(4 A), 1201–1212.

Ekström, G., Nettles, M., & Dziewoński, A. M., 2012. The global CMT project 2004-2010: Centroid-moment tensors for 13,017 earthquakes, *Phys. Earth Planet. Inter.*, **200-201**, 1–9.

Fukuda, J. & Johnson, K. M., 2008. A fully Bayesian inversion for spatial distribution of fault slip with objective smoothing, *Bull. Seismol. Soc. Am.*, **98**(3), 1128–1146.

Hallo, M. & Gallovic, F., 2016. Fast and cheap approximation of Green function uncertainty for waveform-based earthquake source inversions, *Geophys, J. Int.*, **207**, 1012–1029.

Heimann, S., Kriegerowski, M., Isken, M., Cesca, S., Daout, S., Grigoli, F., Juretzek, C., Megies, T., Nooshiri, N., Steinberg, A., Sudhaus, H., Vasyura-Bathke, H., Willey, T., & Dahm, T., 2017. Pyrocko - An open-source seismology toolbox and library, *GFZ Data Services*, **v. 0.3**.

Heimann, S., Vasyura-Bathke, H., Sudhaus, H., Isken, M. P., Kriegerowski, M., Steinberg, A., & Dahm, T., 2019. A Python framework for efficient use of pre-computed Green's functions in seismological and other physical forward and inverse source problems, *Solid Earth*, **10**(6), 1921–1935.

Hofstetter, A., Thio, H. K., & Shamir, G., 2003. Source mechanism of the 22 / 11 / 1995 Gulf of Aqaba earthquake and its aftershock sequence, *J. Seismolog.*, **7**, 99–114.

Holland, C. W., Dettmer, J., & Dosso, S. E., 2005. Remote sensing of sediment density and velocity gradients in the transition layer, *J. Acoust. Soc. Am.*, **118**(1), 163–177.

Hunter, J. D., 2007. Matplotlib : A 2D graphics environment, *Comput. Sci. Eng.*, **9**(3), 90–95.

Jost, M. L. & Herrmann, R. B., 1989. A Student's Guide to and Review of Moment Tensors, *Seismol. Res. Lett.*, **60**(2), 37–57.

Kennett, B. L. N., Engdahl, E. R., & Buland, R., 1995. Constraints on seismic velocities in the Earth from traveltimes, *Geophys, J. Int.*, **122**, 108–124.

Koch, K., 1991. Moment tensor inversion of local earthquake dataII. Application to aftershocks of the May 1980 Mammoth Lakes earthquakes, *Geophys, J. Int.*, **106**(2), 321–332.

Kravanja, S., Panza, G. F., & Šílený, J., 1999. Robust retrieval of a seismic point-source time function, *Geophys, J. Int.*, **136**(2), 385–394.

Minson, S. E., Simons, M., & Beck, J. L., 2013. Bayesian inversion for finite fault earthquake source models I-theory and algorithm, *Geophys, J. Int.*, **194**(3), 1701–1726.

Monelli, D. & Mai, P. M., 2008. Bayesian inference of kinematic earthquake rupture parameters through fitting of strong motion data, *Geophys, J. Int.*, **173**(1), 220–232.

Mooney, W. D., 1989. Seismic methods for determining parameters and lithospheric structure earthquake source, in *Geophysical framework of the United States: Boulder, Colorado*, pp. 71–110, eds Pakiser, L. C. & Mooney, W. D., Geological Society of America Memoir 172.

Moral, P. D., Doucet, A., & Jasra, A., 2006. Sequential Monte Carlo samplers, *J.R. Statist. Soc. B.*, **68**(3), 411–436.

Pugh, D. J., White, R. S., & Christie, P. A., 2016. A Bayesian method for microseismic source inversion, *Geophys, J. Int.*, **206**(2), 1009–1038.

Ragon, T., Sladen, A., & Simons, M., 2018. Accounting for uncertain fault geometry in earthquake source inversions - I: Theory and simplified application, *Geophys, J. Int.*, **214**(2), 1174–1190.

Razafindrakoto, H. N. T. & Mai, M. P., 2014. Uncertainty in earthquake source imaging due to variations in source time function and earth structure, *Bull. Seismol. Soc. Am.*, **104**(2), 855–874.

Sambridge, M. & Mosegaard, K., 2002. Monte Carlo Methods in Geophysical Inverse Problems, *Rev. Geophys.*, **40**(3), 1009.

Schultz, R., Stern, V., Novakovic, M., Atkinson, G., & Gu, Y. J., 2015. Hydraulic fracturing and the Crooked Lake Sequences: Insights gleaned from regional seismic networks, *Geophys. Res. Lett.*, **42**(8), 2750–2758.

505 Sigloch, K. & Nolet, G., 2006. Measuring finite-frequency body-wave amplitudes and traveltimes,
506 *Geophys, J. Int.*, **167**(1), 271–287.
507 Šílen, J., Panza, G. F., & Campus, P., 1992. Waveform inversion for point source moment tensor
508 retrieval with variable hypocentral depth and structural model, *Geophys, J. Int.*, **109**(2), 259–274.
509 Sipkin, S. A., 1982. Estimation of earthquake source parameters by the inversion of waveform data:
510 synthetic waveforms, *Phys. Earth Planet. Inter.*, **30**(2-3), 242–259.
511 Stähler, S. C. & Sigloch, K., 2014. Fully probabilistic seismic source inversion Part 1 : Efficient
512 parameterisation, *Solid Earth*, **5**, 1055–1069.
513 Stähler, S. C. & Sigloch, K., 2016. Fully probabilistic seismic source inversion Part 2 : Modelling
514 errors and station covariances, *Solid Earth*, (7), 1521–1536.
515 Tarantola, A., 2005. *Inverse Problem Theory and methods for model parameter estimation*, SIAM.
516 Tarantola, A. & Valette, B., 1982. Inverse Problems = Quest for Information, *J. Geophys.*, **50**,
517 159–170.
518 Tocheport, A., Rivera, L., & Chevrot, S., 2007. A systematic study of source time functions and
519 moment tensors of intermediate and deep earthquakes, *J. Geophys. Res. Solid Earth*, **112**(7), 1–22.
520 Vackář, J., Burjánek, J., Gallovič, F., Zahradńik, J., & Clinton, J., 2017. Bayesian ISOLA: New tool
521 for automated centroid moment tensor inversion, *Geophys, J. Int.*, **210**(2), 693–705.
522 Vasyura-Bathke, H., Dettmer, J., Steinberg, A., Heimann, S., Isken, M., Zielke, O., Mai, P. M.,
523 Sudhaus, H., & Jónsson, S., 2019. BEAT - Bayesian Earthquake Analysis Tool, *GFZ Data Services*,
524 **v.1.0**.
525 Vasyura-Bathke, H., Dettmer, J., Steinberg, A., Heimann, S., Isken, M. P., Zielke, O., Mai, P. M.,
526 Sudhaus, H., & Jónsson, S., 2020. The Bayesian Earthquake Analysis Tool, *Seismol. Res. Lett.*,
527 **91**(2A), 1003–1018.
528 Wang, R., Gu, Y. J., Schultz, R., Kim, A., & Atkinson, G., 2016. Source analysis of a potential
529 hydraulic-fracturing-induced earthquake near Fox Creek, Alberta, *Geophys. Res. Lett.*, **43**(2), 564–
530 573.
531 Wéber, Z., 2006. Probabilistic local waveform inversion for moment tensor and hypocentral location,
532 *Geophys, J. Int.*, **165**(2), 607–621.
533 Wessel, P., Smith, W. H. F., Scharroo, R., Luis, J., & Wobbe, F., 2013. Generic Mapping Tools:
534 Improved Version Released, *EOS Trans. AGU*, **94**(45), 409–410.
535 Yagi, Y. & Fukahata, Y., 2008. Importance of covariance components in inversion analyses of densely
536 sampled observed data : an application to waveform data inversion for seismic source processes,
537 *Geophys, J. Int.*, **175**, 215–221.

538 Yagi, Y. & Fukahata, Y., 2011. Introduction of uncertainty of Green's function into waveform inversion
539 for seismic source processes, *Geophys, J. Int.*, **186**(2), 711–720.

7 TABLES

Table 1. Noise parameterisations used in this study. The data covariance matrix $\mathbf{C}_k^d$, can be estimated from waveform data before the arrival time of the event of interest.

Noise parameterisation	Covariance matrix components	Color coding	References
variance	$\mathbf{C}^d = \sigma^2\mathbf{I}$	light yellow	
exponential	$\mathbf{C}_{ij}^d = \sigma^2 \exp -\lvert\Delta t^{ij}\rvert/t_0$	light blue	Duputel et al. (2012)
variance_cov	$\mathbf{C}^d + \mathbf{C}^t$	dark yellow	Tarantola & Valette (1982); Yagi & Fukahata (2011); Duputel et al. (2014)
exponential_cov	$\mathbf{C}_{ij}^d + \mathbf{C}^t$	dark blue	Tarantola & Valette (1982); Yagi & Fukahata (2011); Duputel et al. (2014)
non-Toeplitz	$\mathbf{C}$	red	Dettmer et al. (2007)

Table 2. Synthetic tests setup cases.

Setup case	velocity structures	
	reference	estimation
1.small theory error	blue	dark gray
2.large theory error	red	dark gray

Table 3. Target source parameters of the double-couple moment tensor.

Synthetic tests				
	moment tensor			
location	east-shift [km]	10.0		
	north-shift [km]	20.0		
	depth [km]	8.0		
strength	magnitude	4.8		
timing	source time [s]	-2.7		
mechanism	mnn	0.846	strike [deg]	150.0
	mee	-0.759	dip [deg]	75.0
	mdd	-0.087	rake [deg]	-10.0
	mne	0.513		
	mnd	0.146		
	med	-0.257		

8 FIGURES

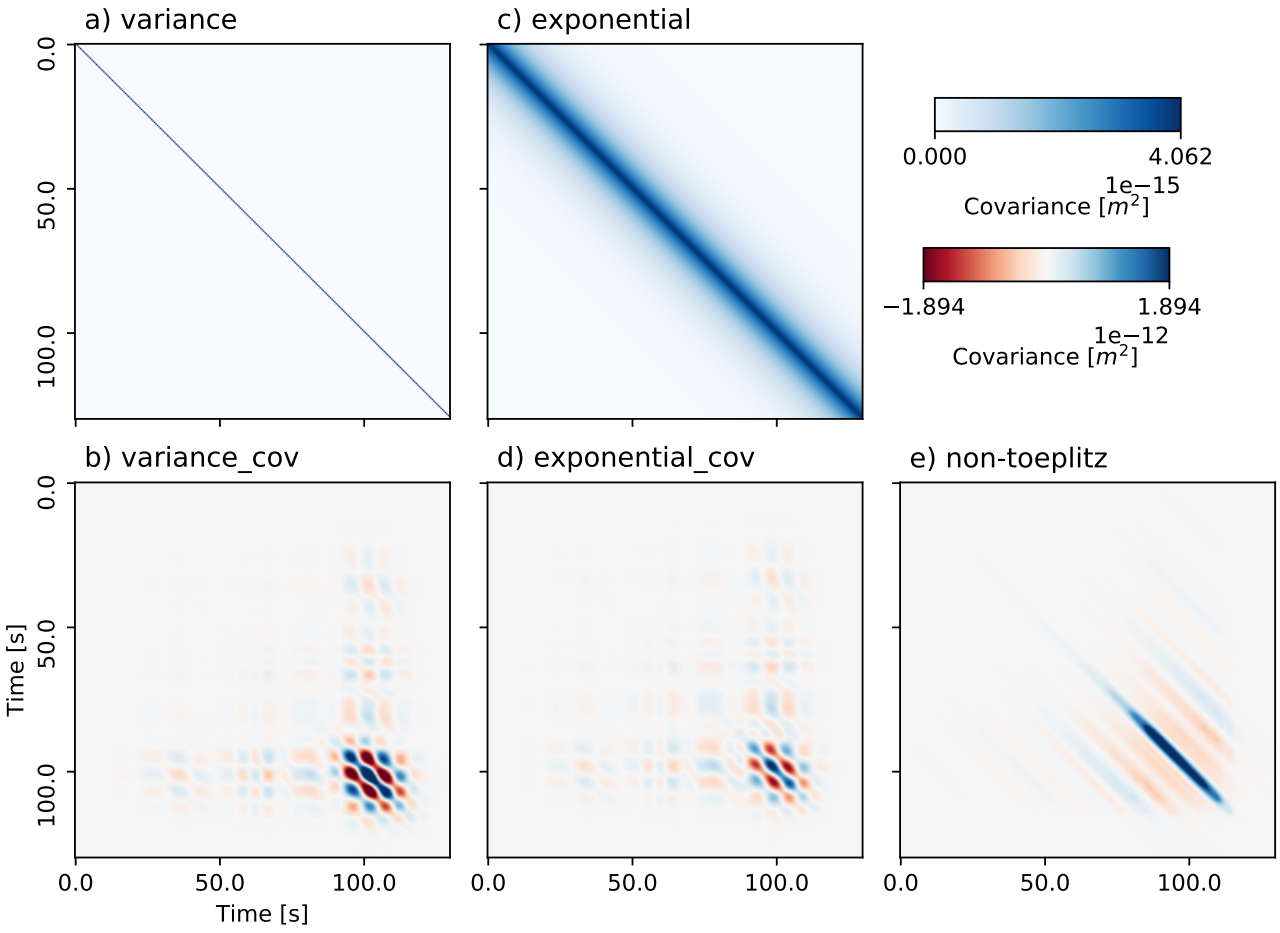

Figure 1. Covariance matrixes $\mathbf{C}$ with different noise parameterisations (Tab. 1). The parameterisations in a) and c) comprise only $\mathbf{C}_k^d$ while b), d) and e) also include $\mathbf{C}_k^t$, thus the ranges of covariance matrix values vary significantly.

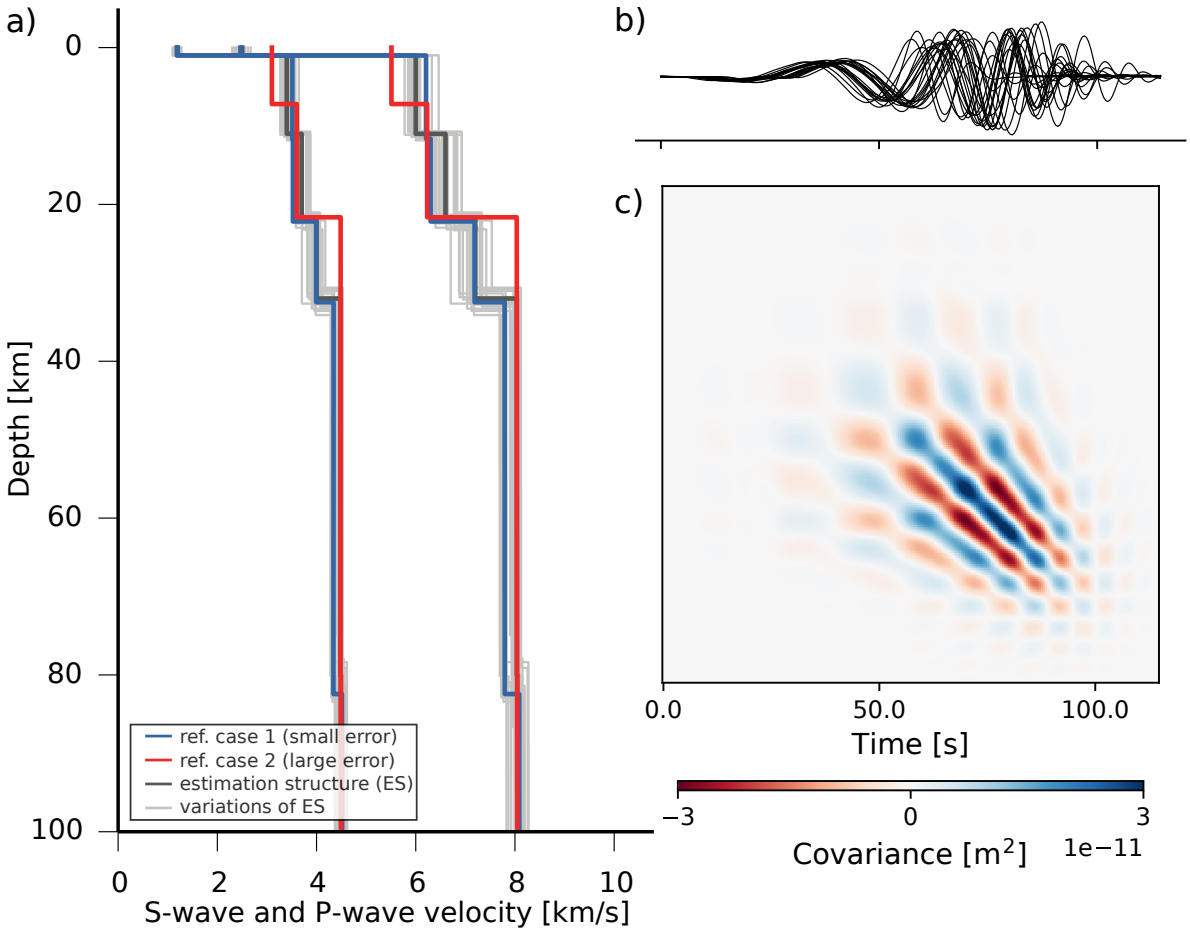

Figure 2. Steps to calculate the model prediction covariance; a) velocity model profiles: b) synthetic waveforms (vertical component) for the reference source simulated for each realization of the Earth structures; c) Covariance matrix $\mathbf{C}_k^t$ of seismic traces from b) following eq. 3.

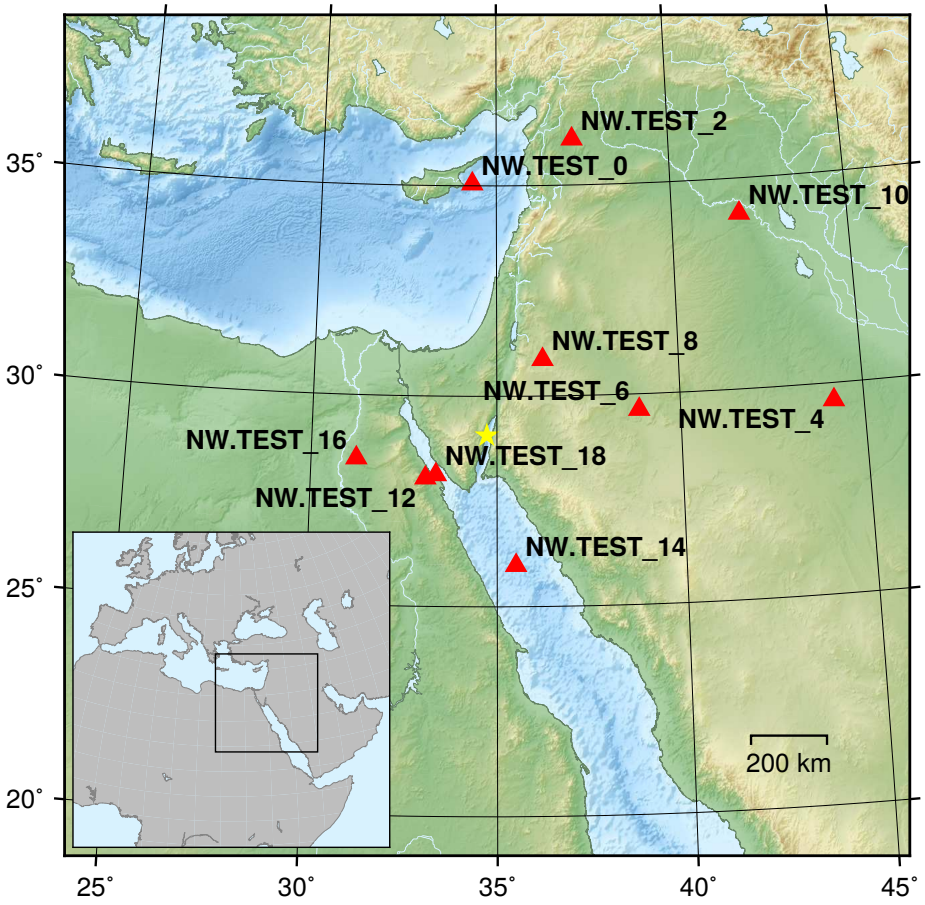

Figure 3. Stations (red triangles) used in the synthetic test that simulates a moment tensor optimization at regional distances. Station locations are randomly chosen around the reference event marked by the yellow star. The black box in the inset marks the outline of the station map.

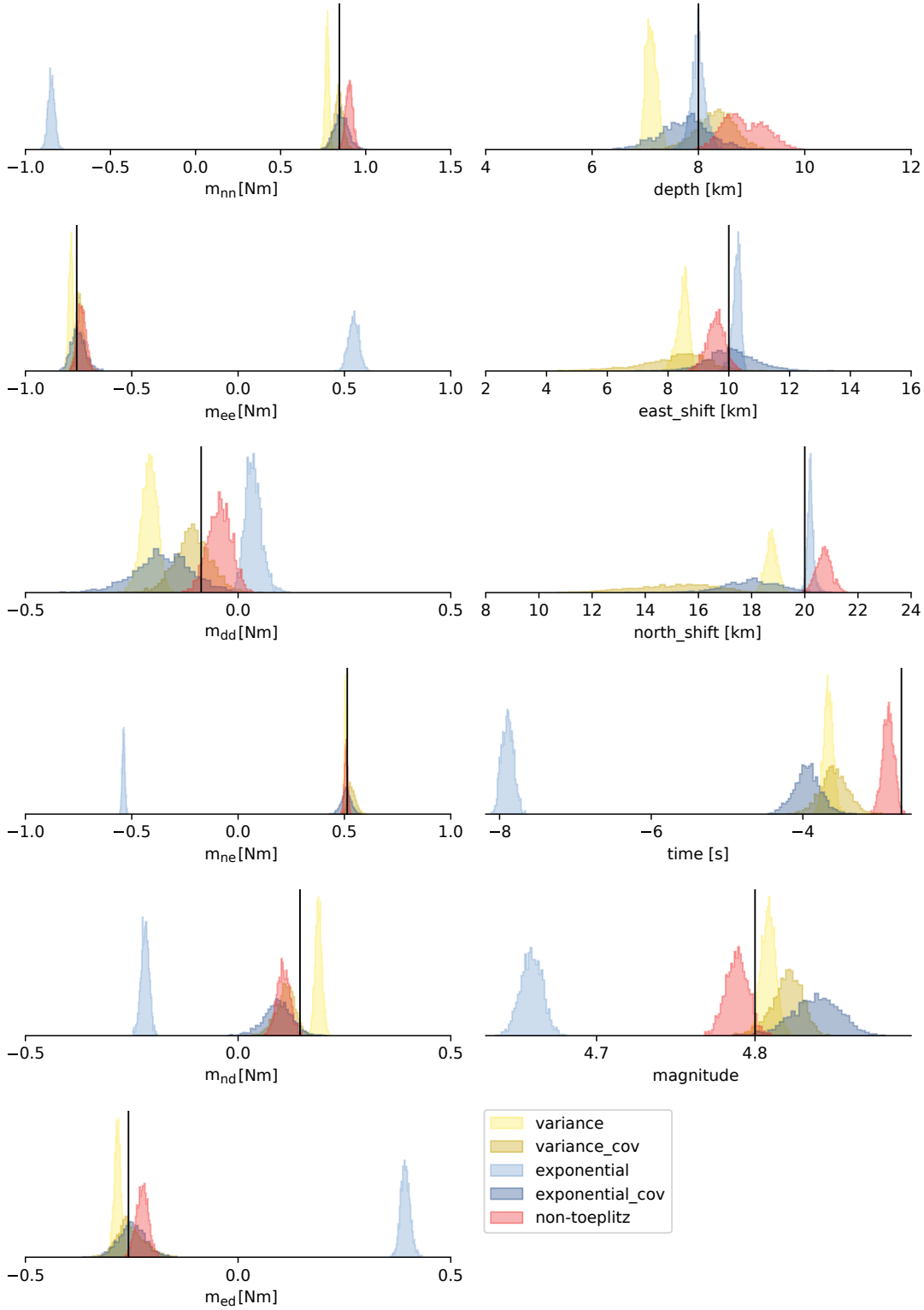

Figure 4. Case 1 with small theory error: histograms of the posterior marginal distributions for the parameters of a full moment tensor. The different colors of the histograms mark the results for different noise parameterisations (see legend). (Table 2).

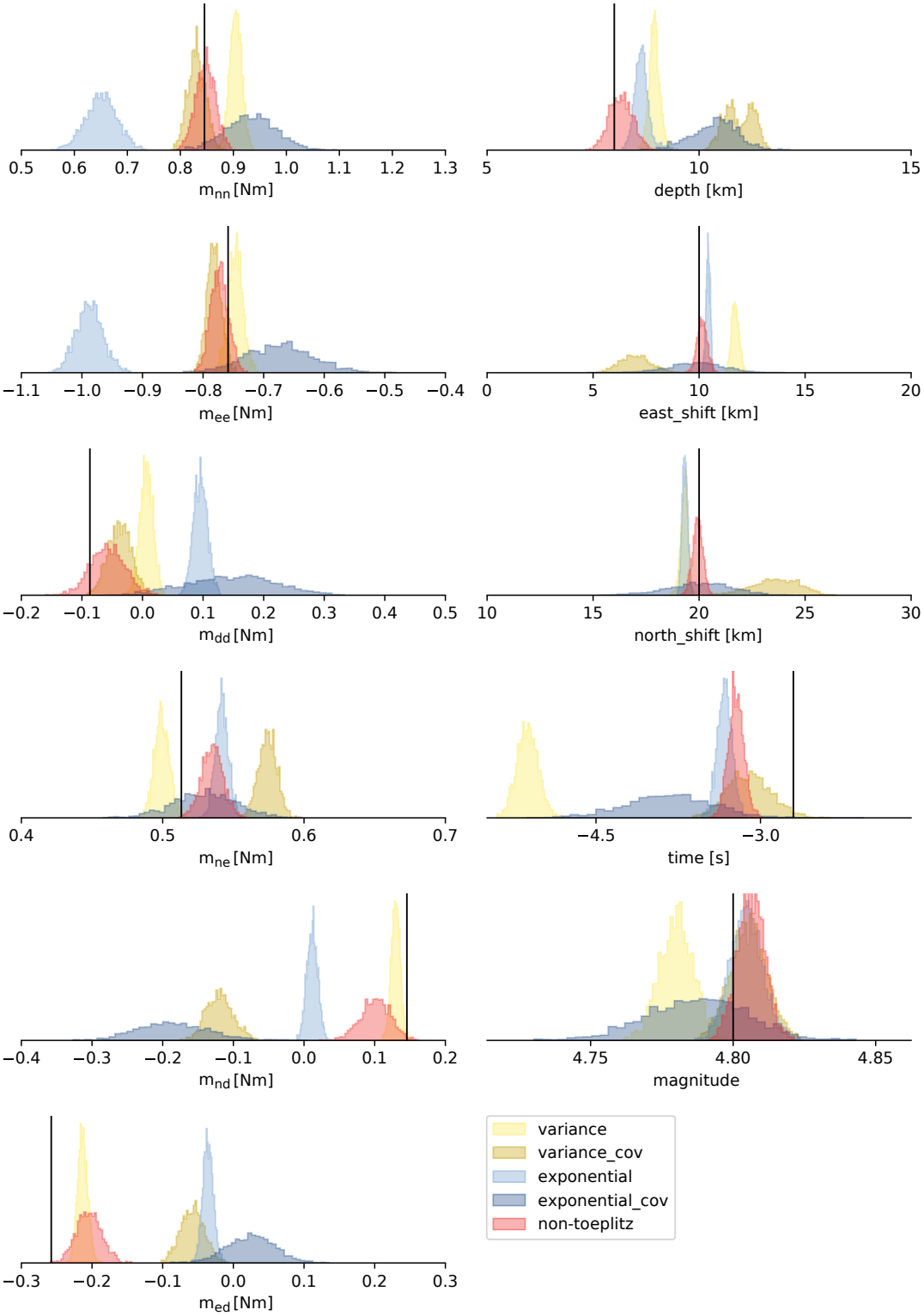

Figure 5. Case 2 with large theory error: histograms of the posterior marginal distributions for the parameters of a full moment tensor. The different colors of the histograms mark the results for different noise parameterisations (see legend). (Table 2).

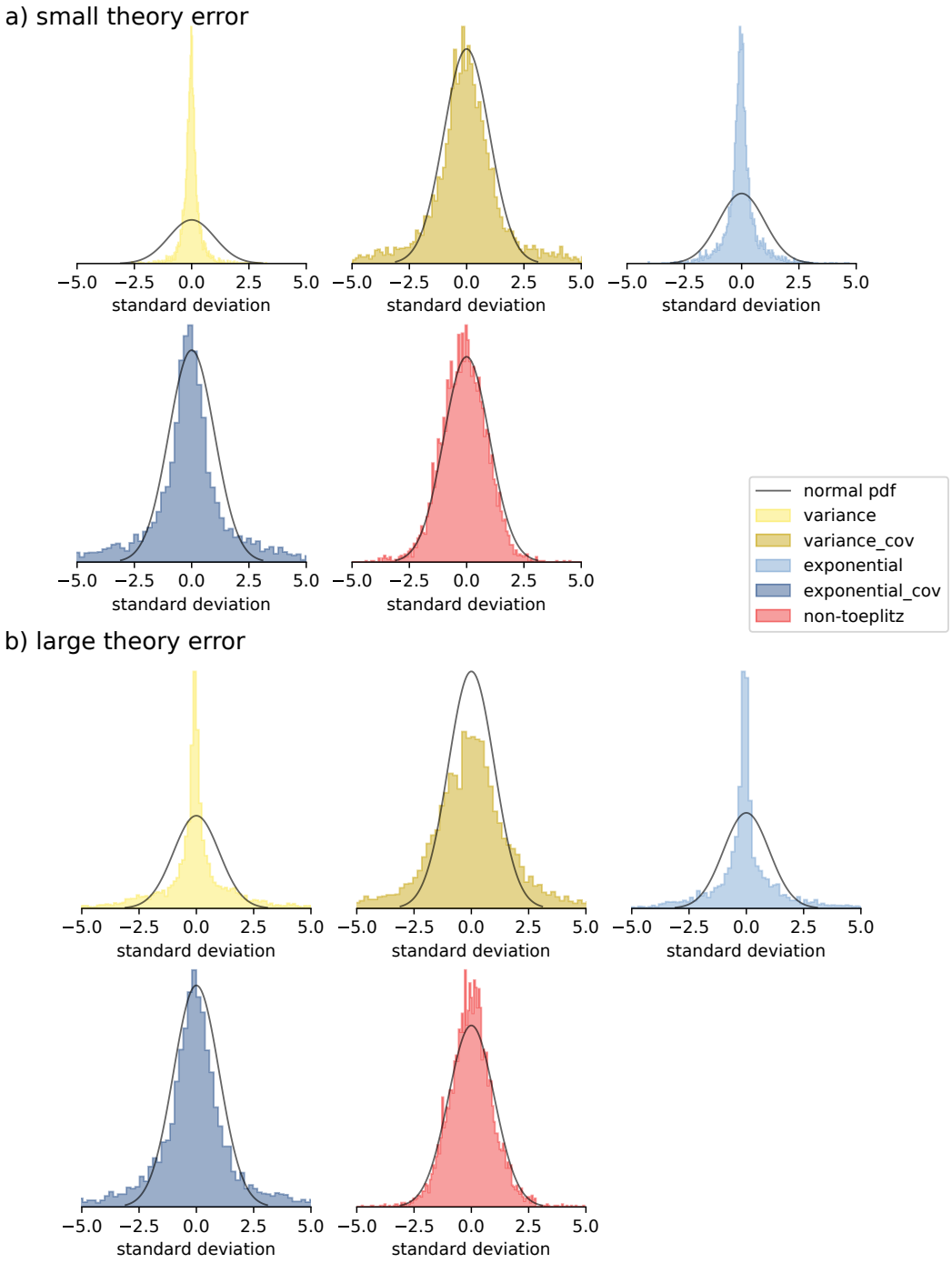

Figure 6. Standardized residuals for the different noise parameterisations for a) small theory error and b) large theory error. The black line marks the analytic normal distribution with zero mean and standard deviation of one. All histograms are normalized.

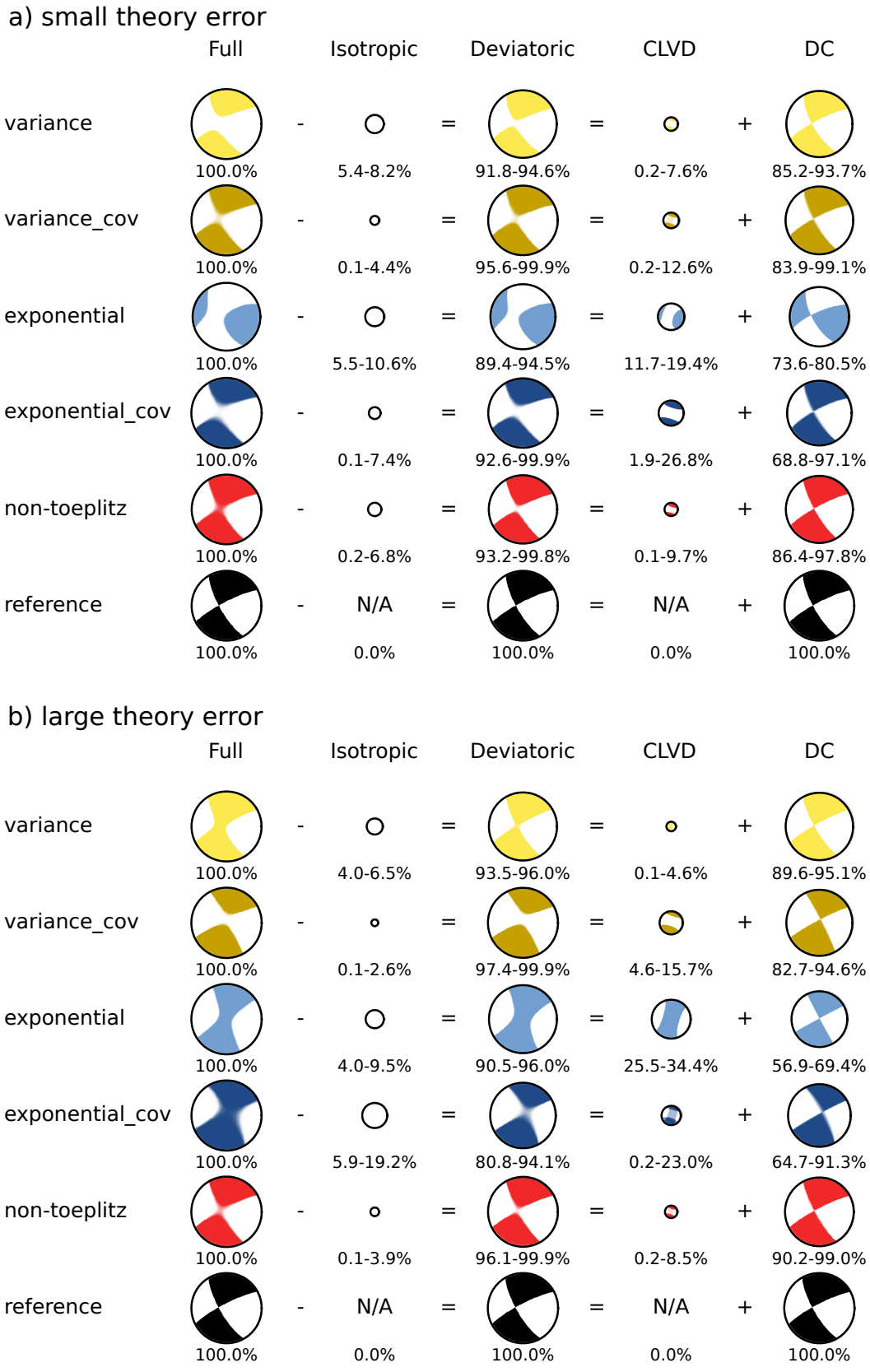

Figure 7. Moment tensor decompositions for a) case 1 with small theory error and for b) case 2 with large theory error. Each row shows the decomposition for a different noise parameterisation following the color-coding in Tab. 1 and Fig. 6. The sizes of the focal mechanisms are scaled with respect to MAP magnitudes.

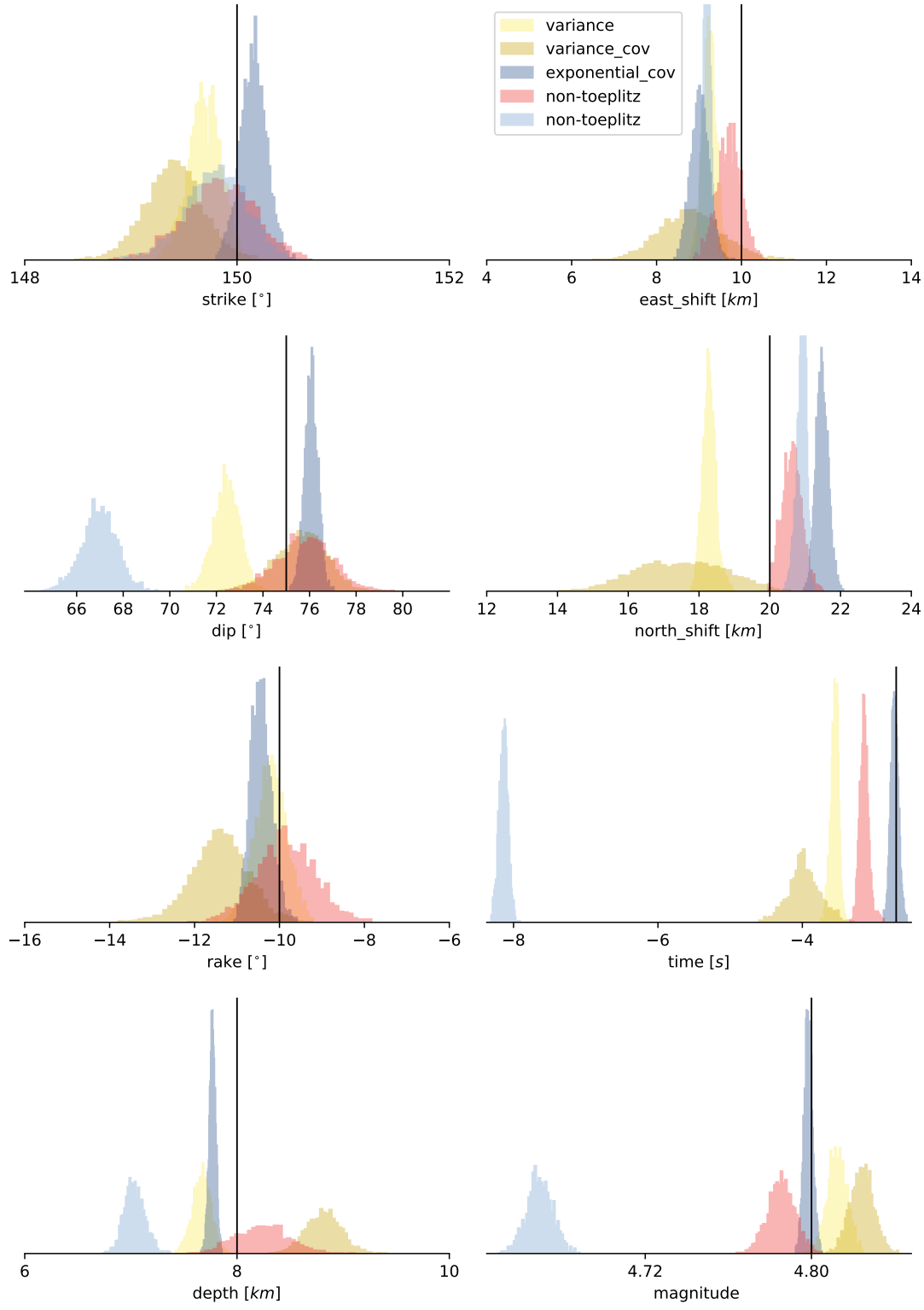

Figure 8. Double-couple moment tensor with small theory error: histograms of the posterior marginal distributions for the parameters of a double-couple moment tensor. The marginal for the rake for the *exponential* case is omitted here, as it is far off the displayed interval at a rake of 155-160. Different colors of the histograms mark results for different noise parameterisations (see legend). (Table 2).

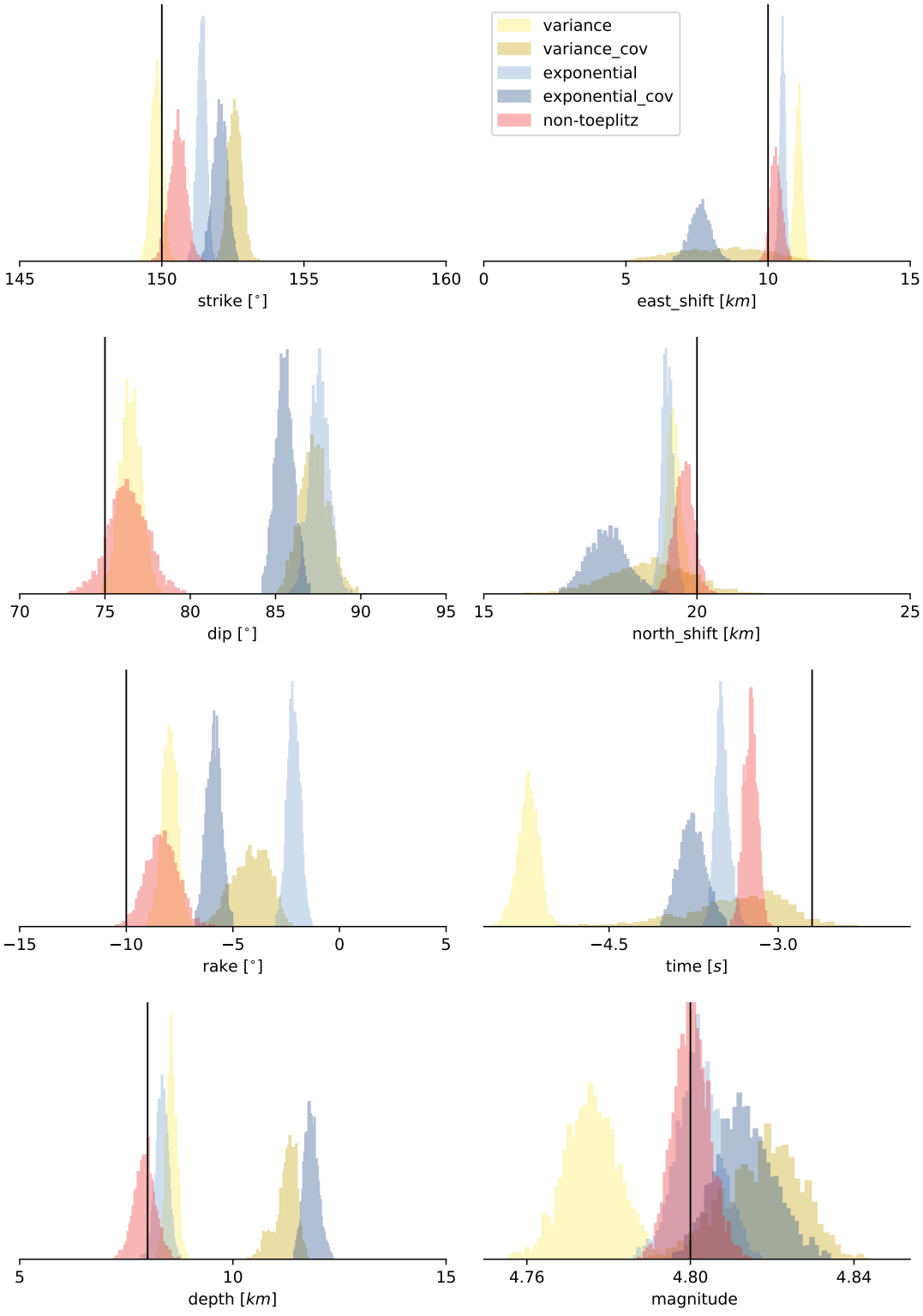

Figure 9. Double-couple moment tensor with large theory error: histograms of the posterior marginal distributions for the parameters of a double-couple moment tensor. The different colors of the histograms mark results for different noise parameterisations (see legend). (Table 2).

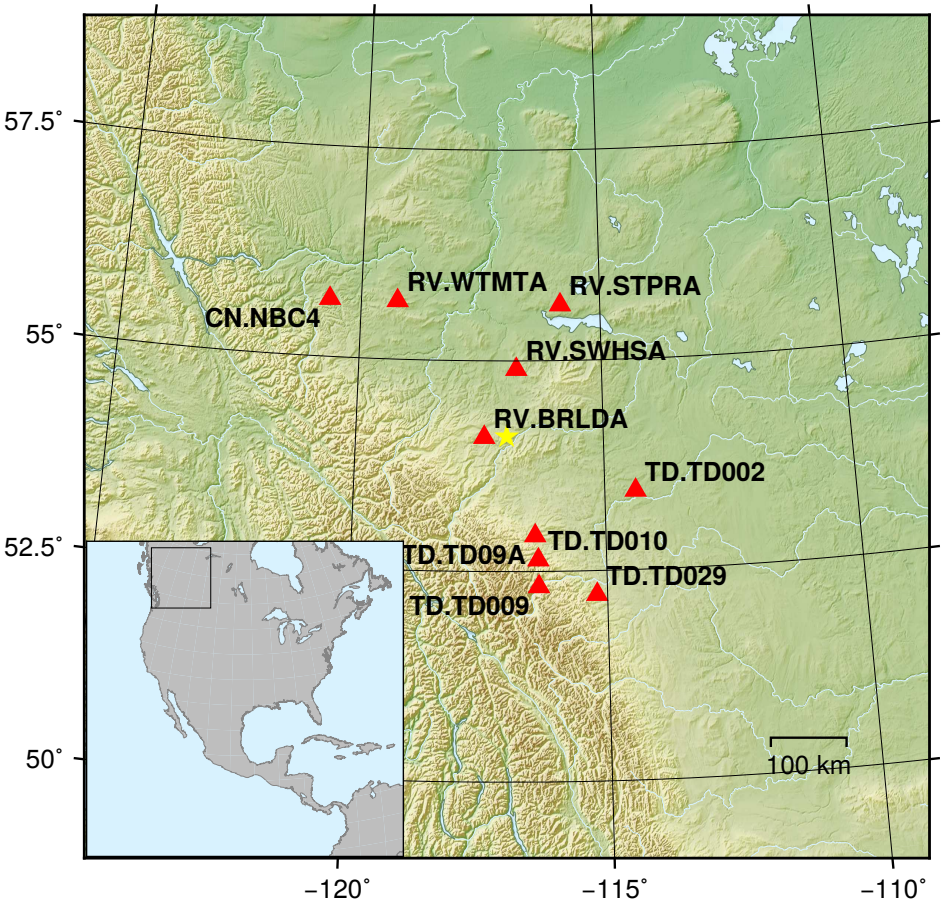

Figure 10. Stations (red triangles) used in the full moment tensor estimation at regional distances for the 13th June 2015 Fox Creek event (yellow star at latitude 54.102° and longitude -116.95°). The black box in the inset marks the outline of the station map.

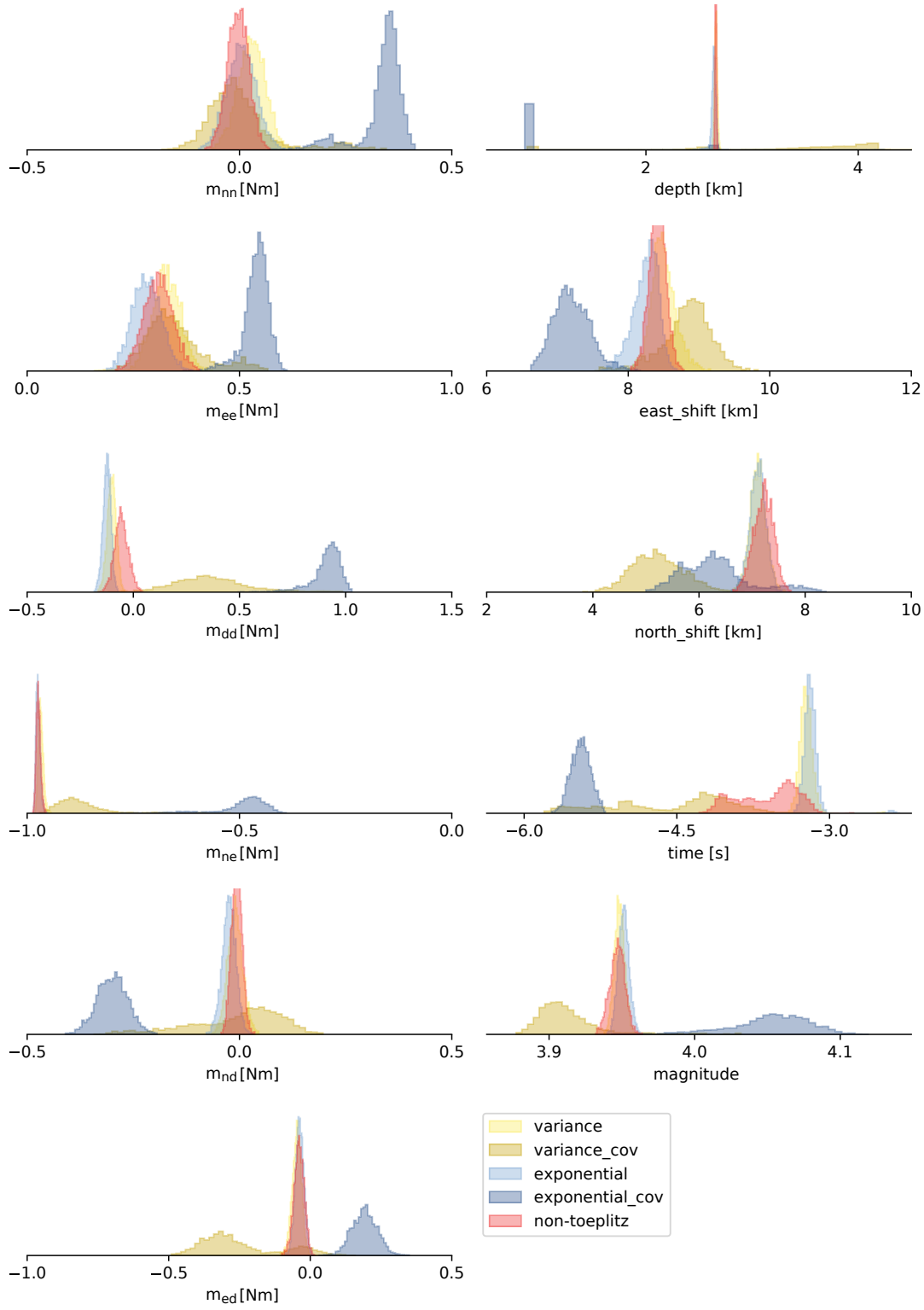

Figure 11. Histograms for the study of the Fox Creek 2015 event with regional Earth structure, showing the posterior marginal distributions for the parameters of a full moment tensor. The location estimates are relative to the reference location from the gCMT catalog at latitude 54.102° and longitude -116.95°. Different colors of the histograms mark results for different noise parameterisations (see legend). (Table 2).

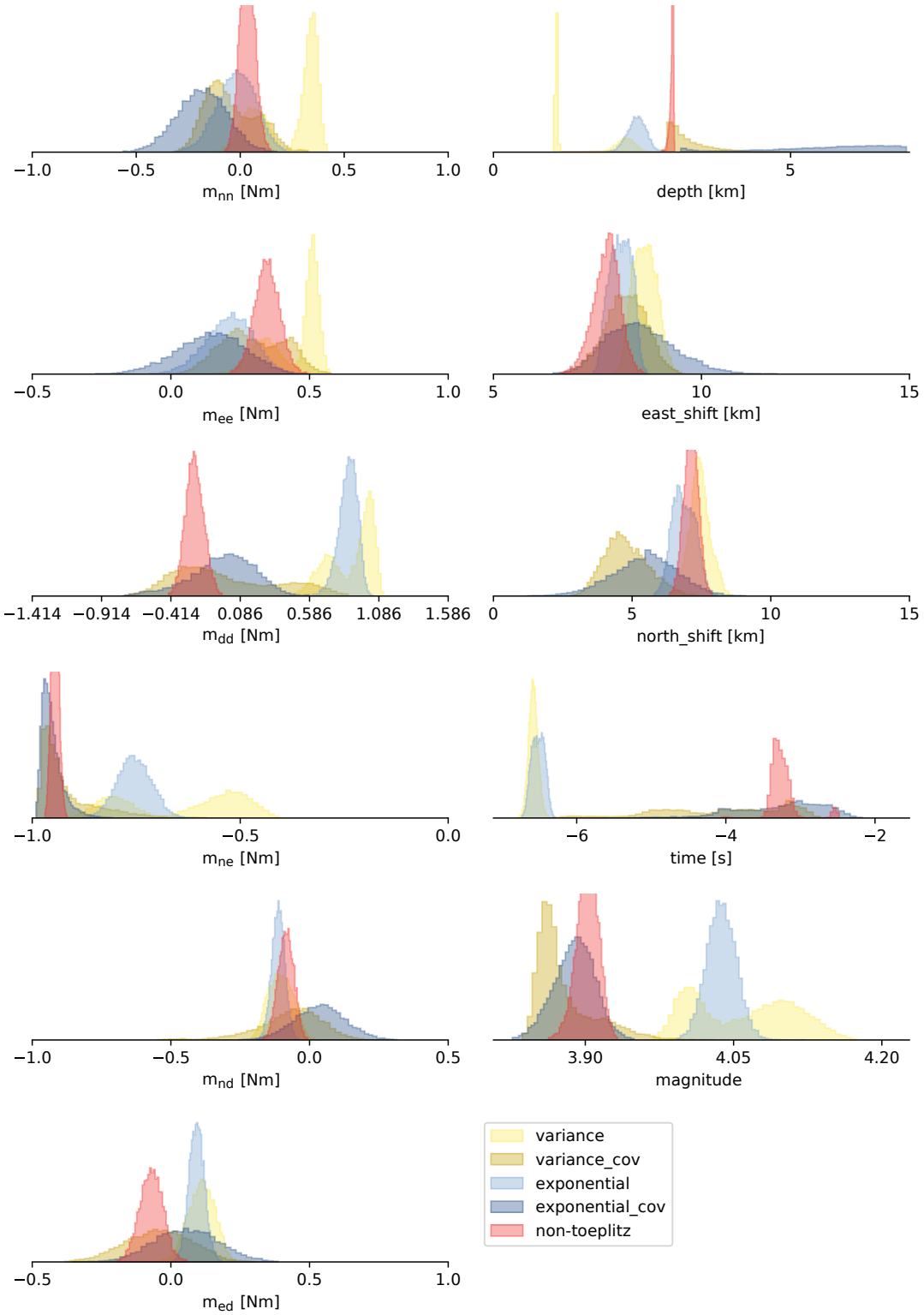

Figure 12. Histograms for the study of the Fox Creek 2015 event with global Earth structure. For details see Fig. 11.

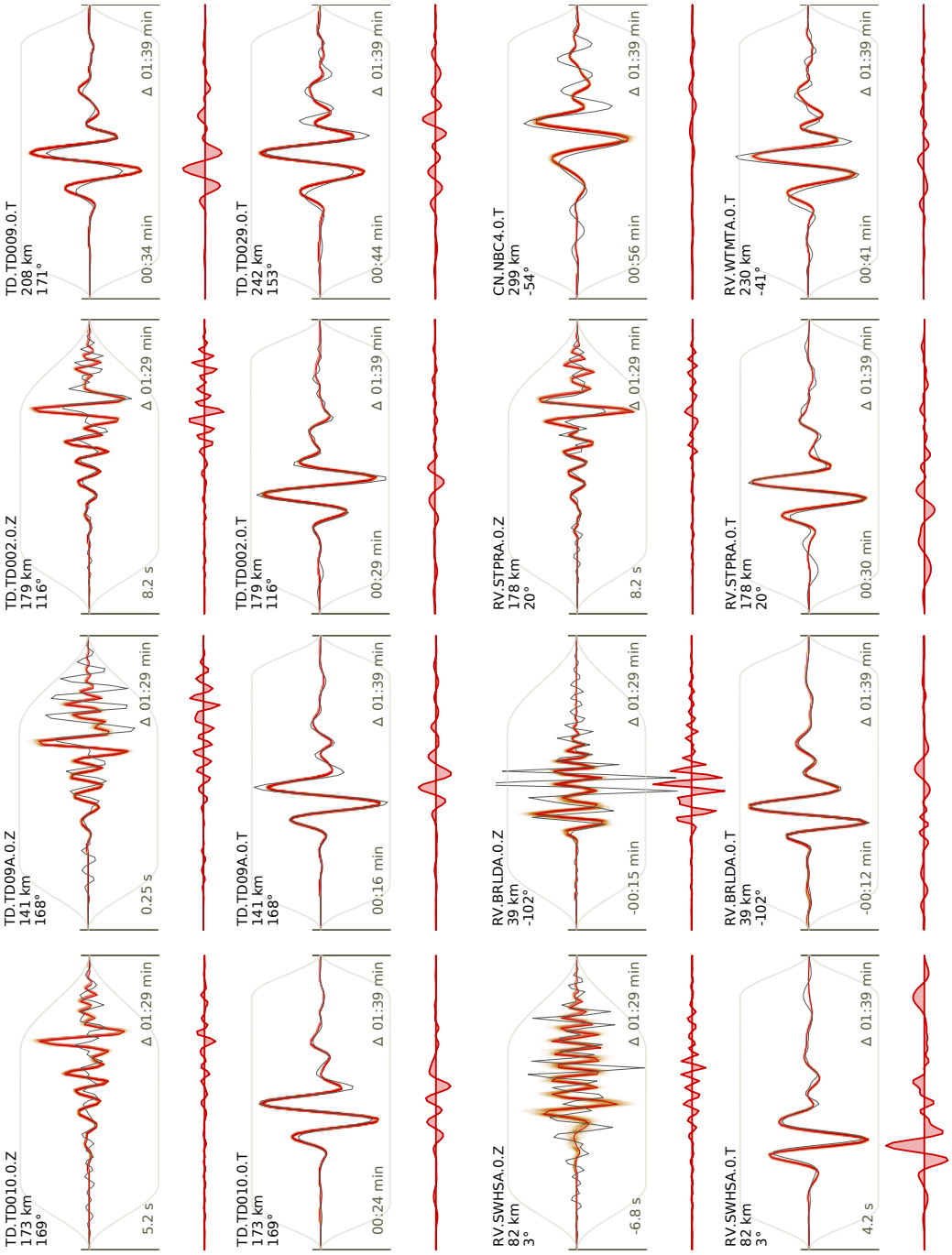

Figure 13. Waveform fits for the full moment tensor solution with *variance* noise parameterisation using the regional subsurface structure. The filtered displacement waveform data (dark grey solid line) for body (Z-component 0.08-0.3Hz) or surface wave arrivals (T-component 0.04-0.1Hz) and filtered synthetic displacement waveforms (red solid line) are shown together, with brown shading indicating 100 random draws of the filtered synthetic displacements from the PPD. The residual waveforms are shown below each waveform as filled red-line polygons. Each trace is annotated with the station name and component, as well as the distance and azimuth from the maximum a-posterior solution of the moment tensor location. The arrival time wrt. the centroid time and the duration of each window are shown in the lower left and right, respectively.

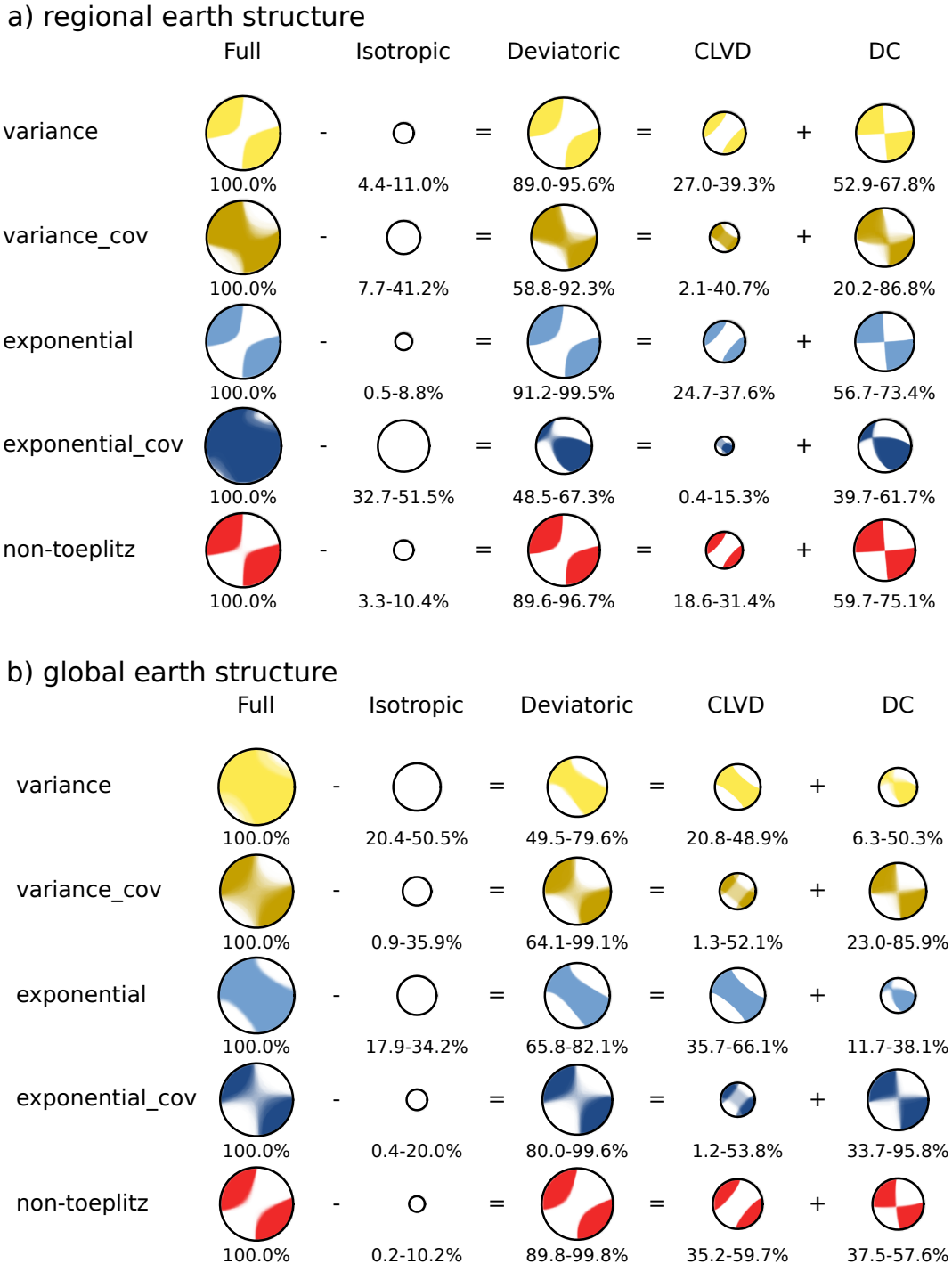

Figure 14. Fox Creek 2015: Moment tensor decompositions of the estimation results from different noise parameterisations for a) regional Earth structure and b) global Earth structure. See also Fig. 7 for complete caption.

9 SUPPLEMENTAL MATERIAL

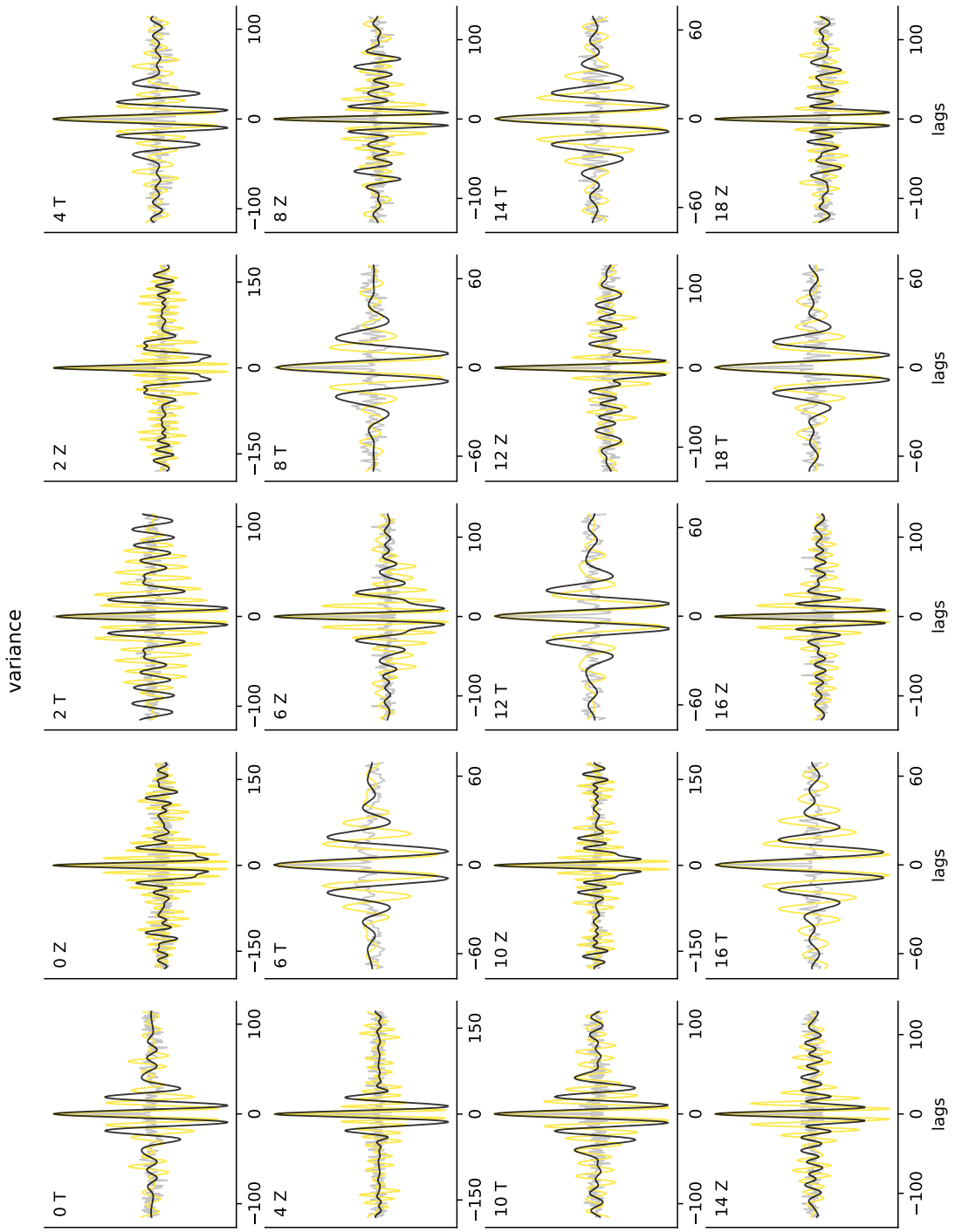

Figure S1. *Variance* parameterisation: Autocorrelations of raw residuals(black), random white noise (light gray) and standardized residuals (colored) of each component and station (shown in the upper left of each subplot).

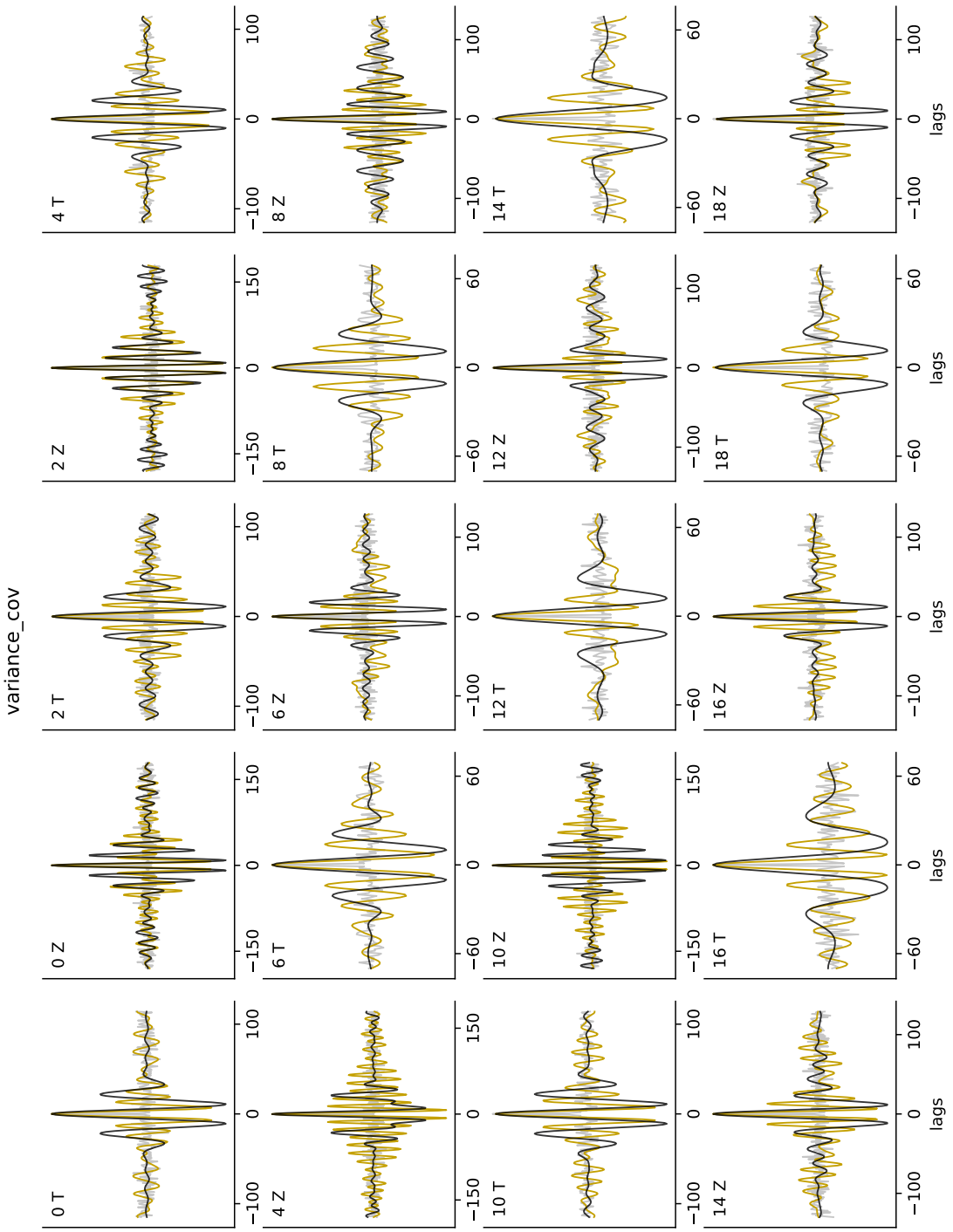

Figure S2. *Variance_cov* parameterisation: Details are described in Fig. S1.

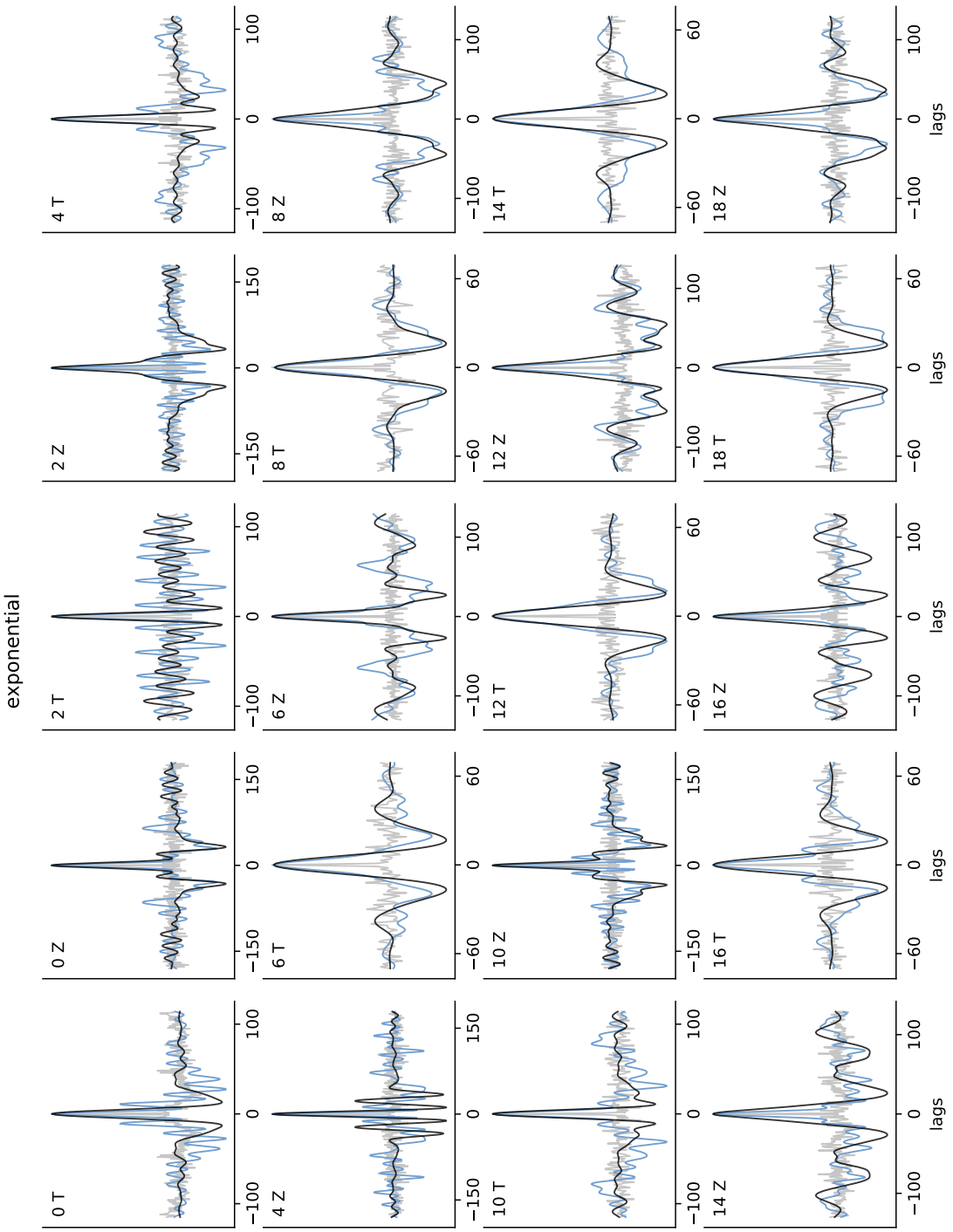

Figure S3. *Exponential* parameterisation: Details are described in Fig. S1.

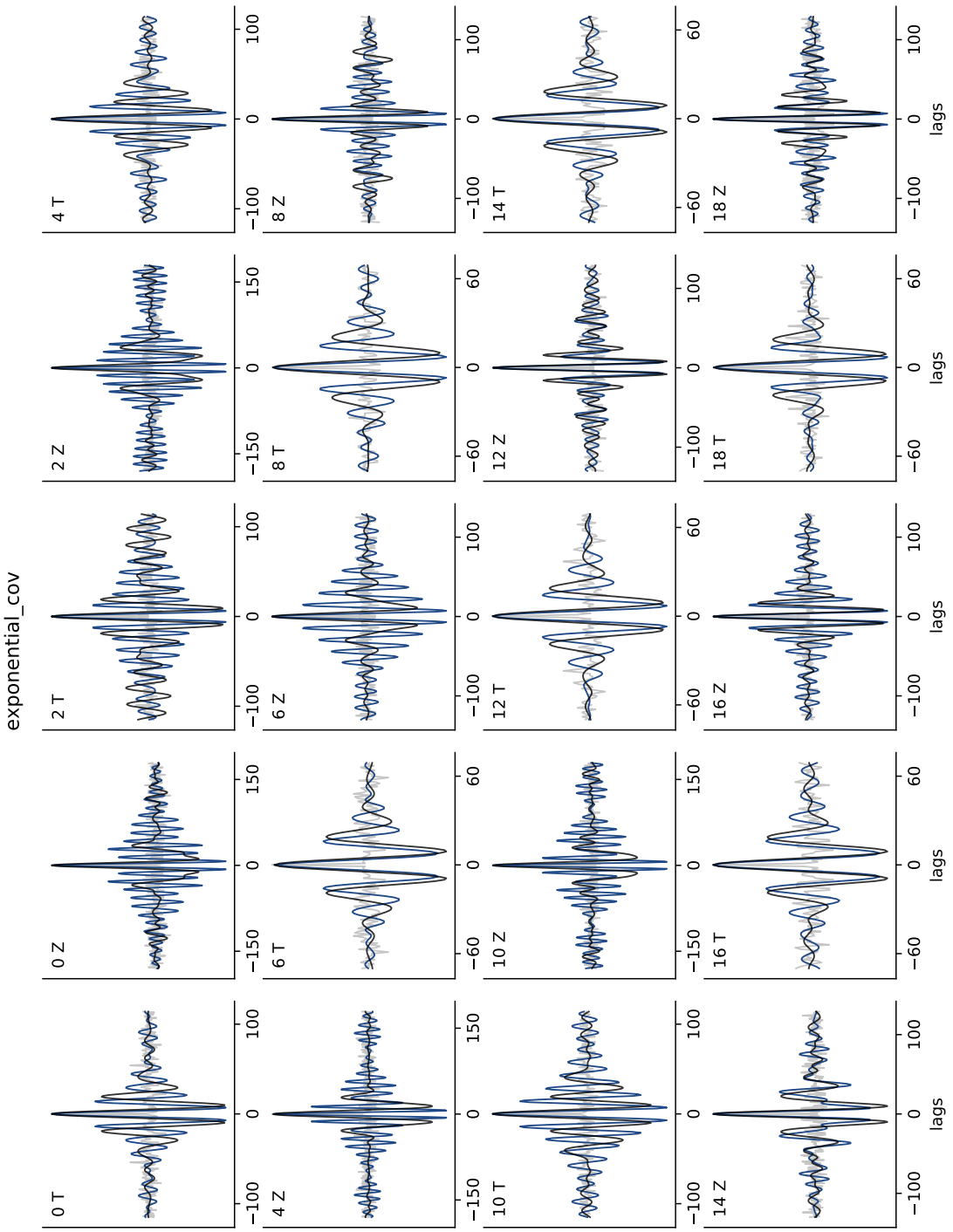

Figure S4. *Exponential_cov* parameterisation: Details are described in Fig. S1.

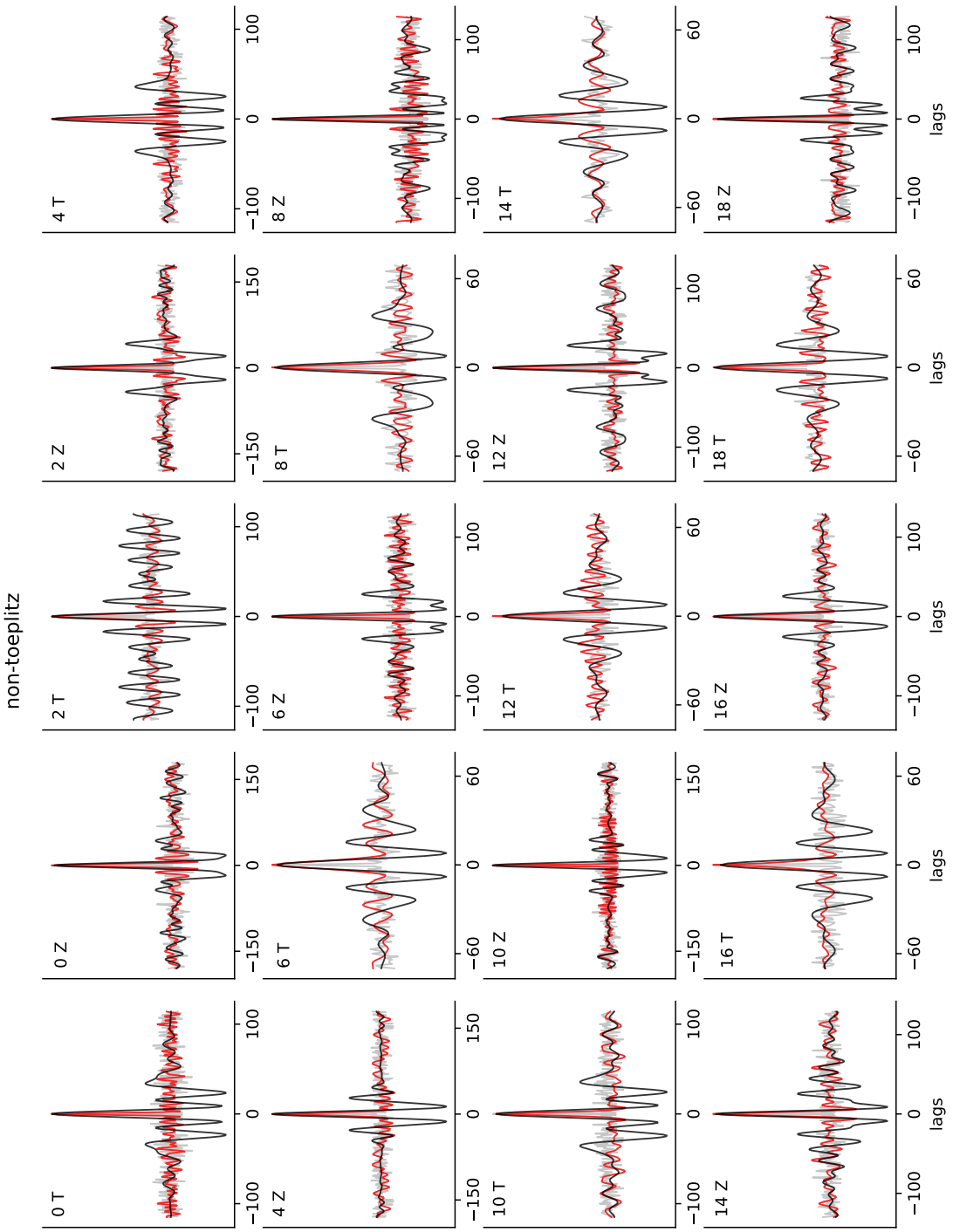

Figure S5. *non-Toeplitz* parameterisation: Details are described in Fig. S1.

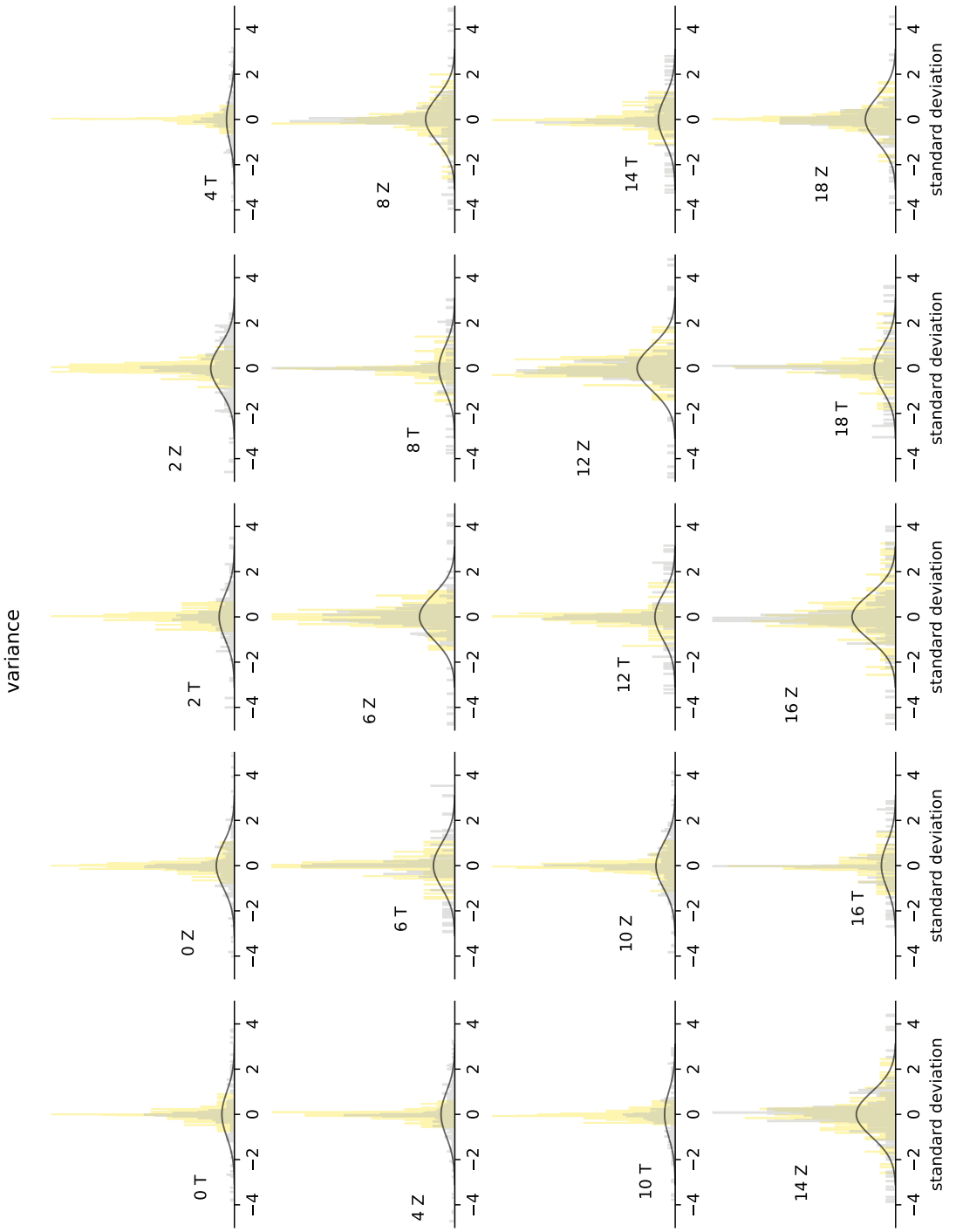

Figure S6. *Variance* parameterisation: Histograms of raw-residuals (light gray), standardized residuals (colored), analytical Gaussian of zero mean and one-sigma standard-deviation (black).

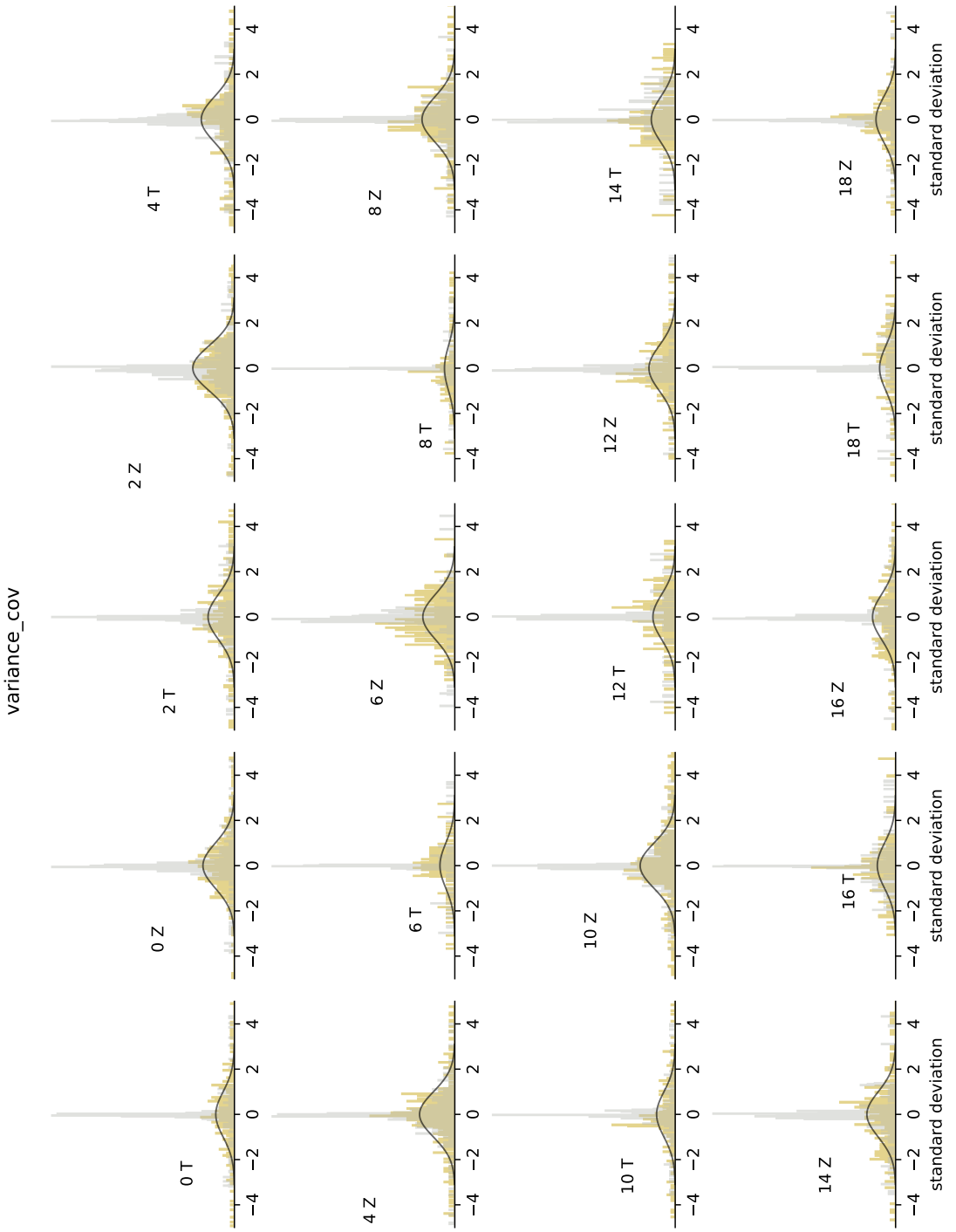

Figure S7. *Variance_cov* parameterisation: Details are described in Fig. S6.

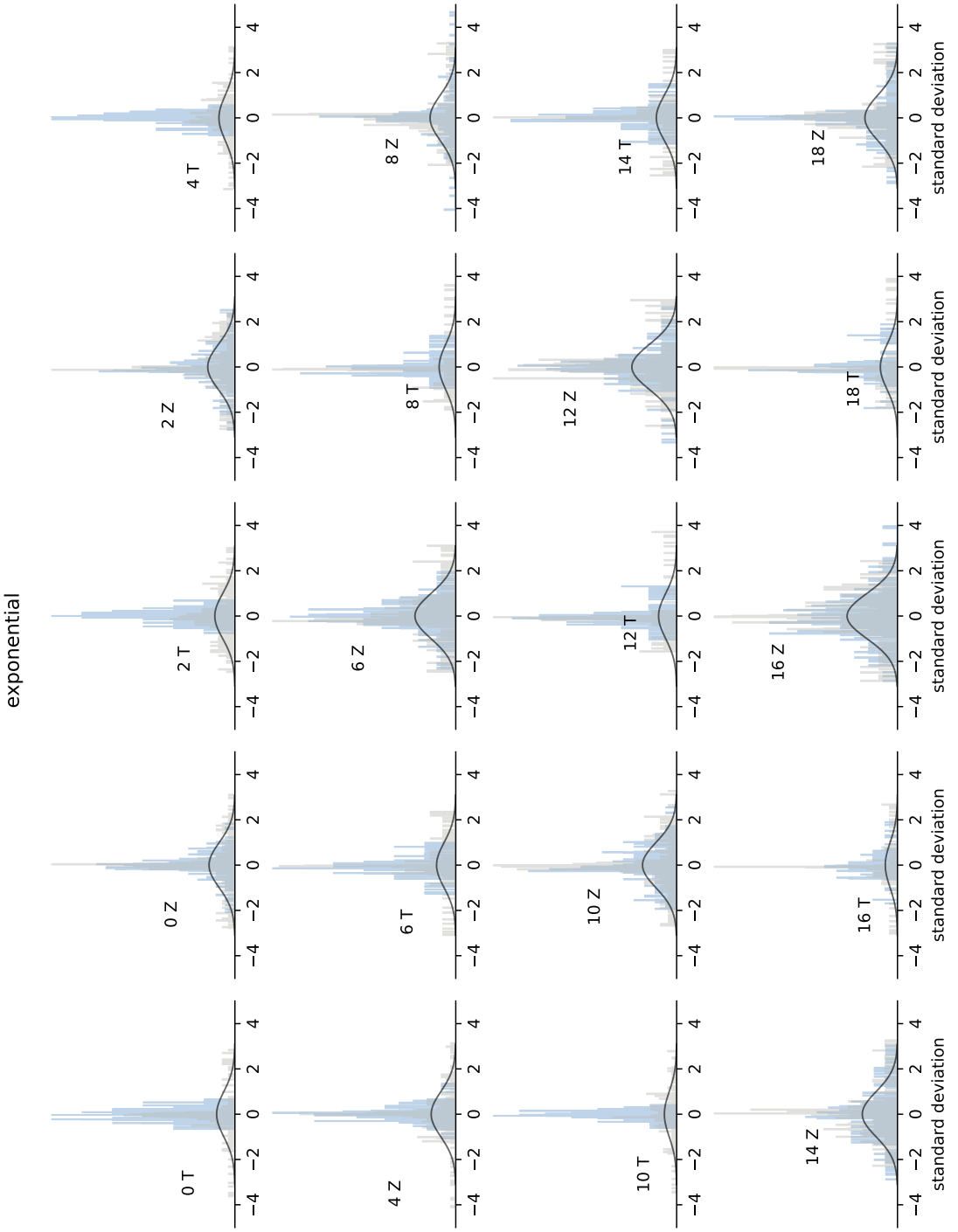

Figure S8. *Exponential* parameterisation: Details are described in Fig. S6.

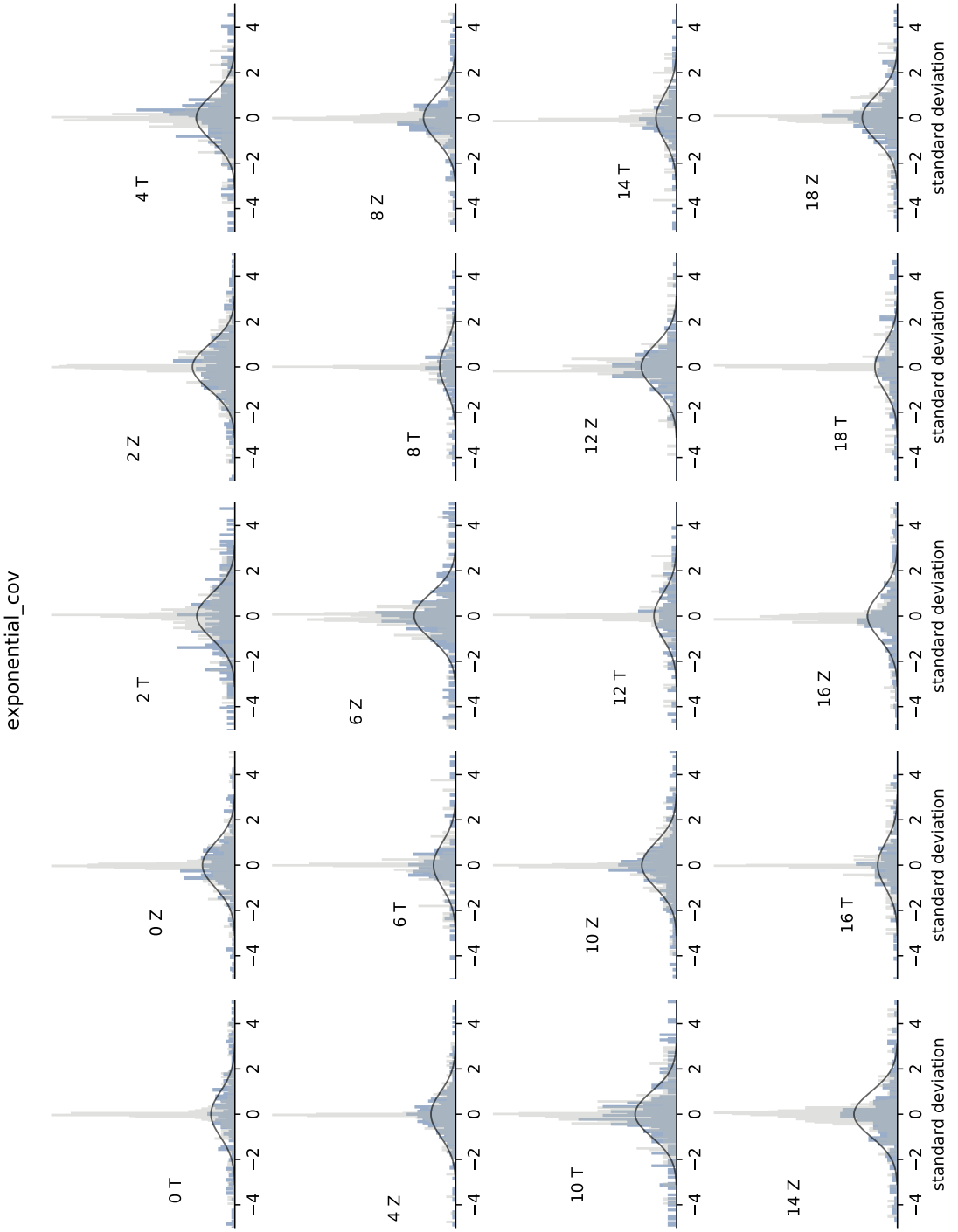

Figure S9. *Exponential_cov* parameterisation: Details are described in Fig. S6.

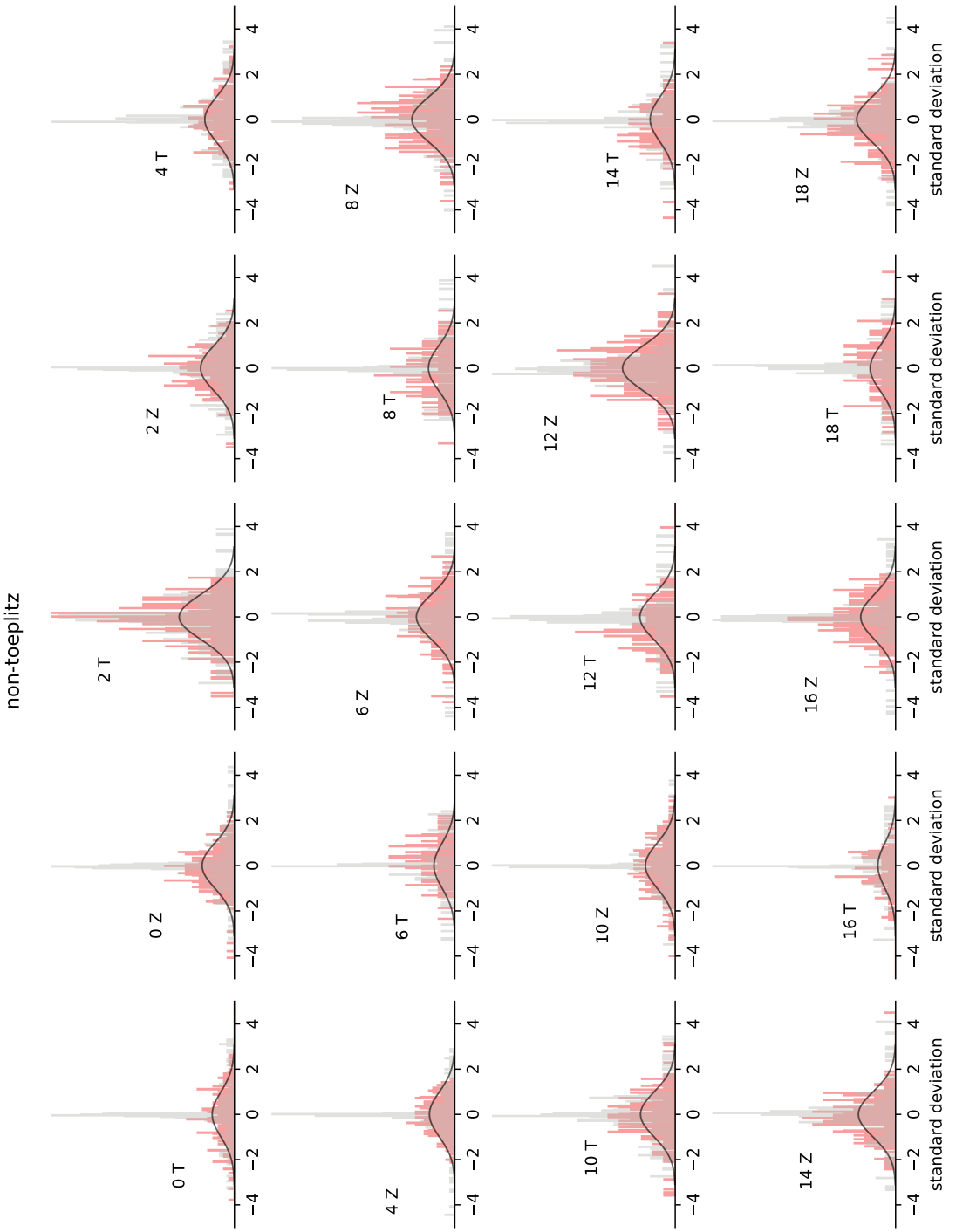

Figure S10. *non-Toeplitz* parameterisation: Details are described in Fig. S6.

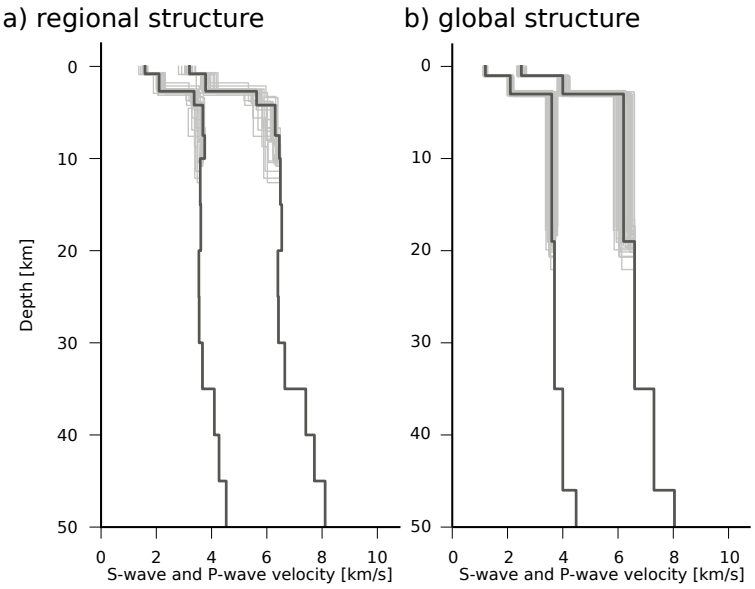

Figure S11. Earth structures (dark gray) a) regional (Wang et al. 2016) and b) global ak135 (Kennett et al. 1995) and their variations (light gray) that have been used in the full moment tensor estimation of the Fox Creek event.

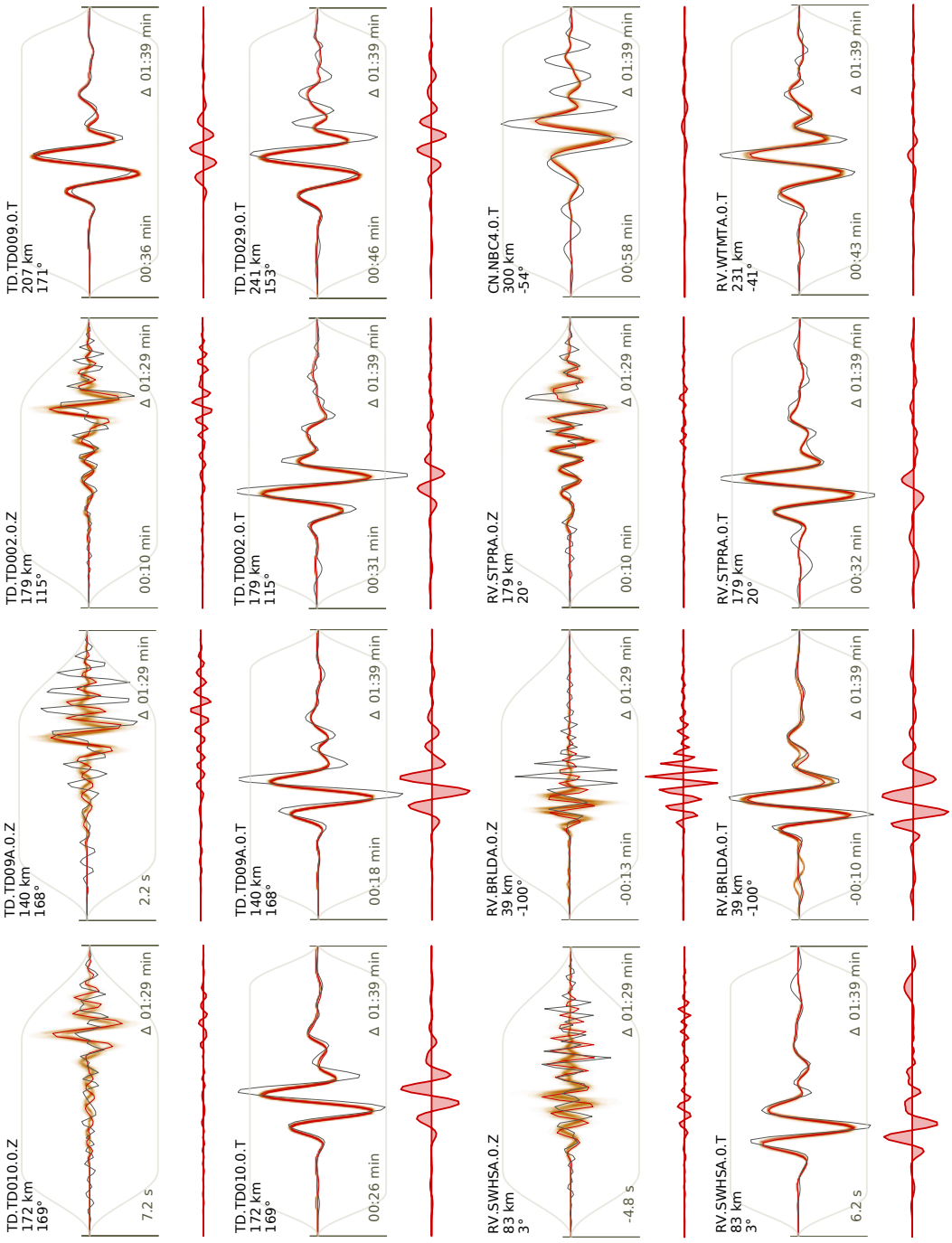

Figure S12. Waveform fits for the full moment tensor solution with *variance_cov* noise parameterisation using the regional subsurface structure. The filtered displacement waveform data (dark grey solid line) for body (Z-component 0.08-0.3Hz) or surface wave arrivals (T-component 0.04-0.1Hz) and the filtered synthetic displacement waveforms (red solid line) are shown together, with the brown shading indicating 100 random draws of the filtered synthetic displacements from the PPD. The residual waveforms are shown below each waveform as filled red-line polygons. Each trace box is annotated with the station name and component, as well as the distance and azimuth from the maximum a-posterior solution of the moment tensor location. The arrival time wrt. the centroid time and the duration of each window are shown in the lower left and right, respectively.

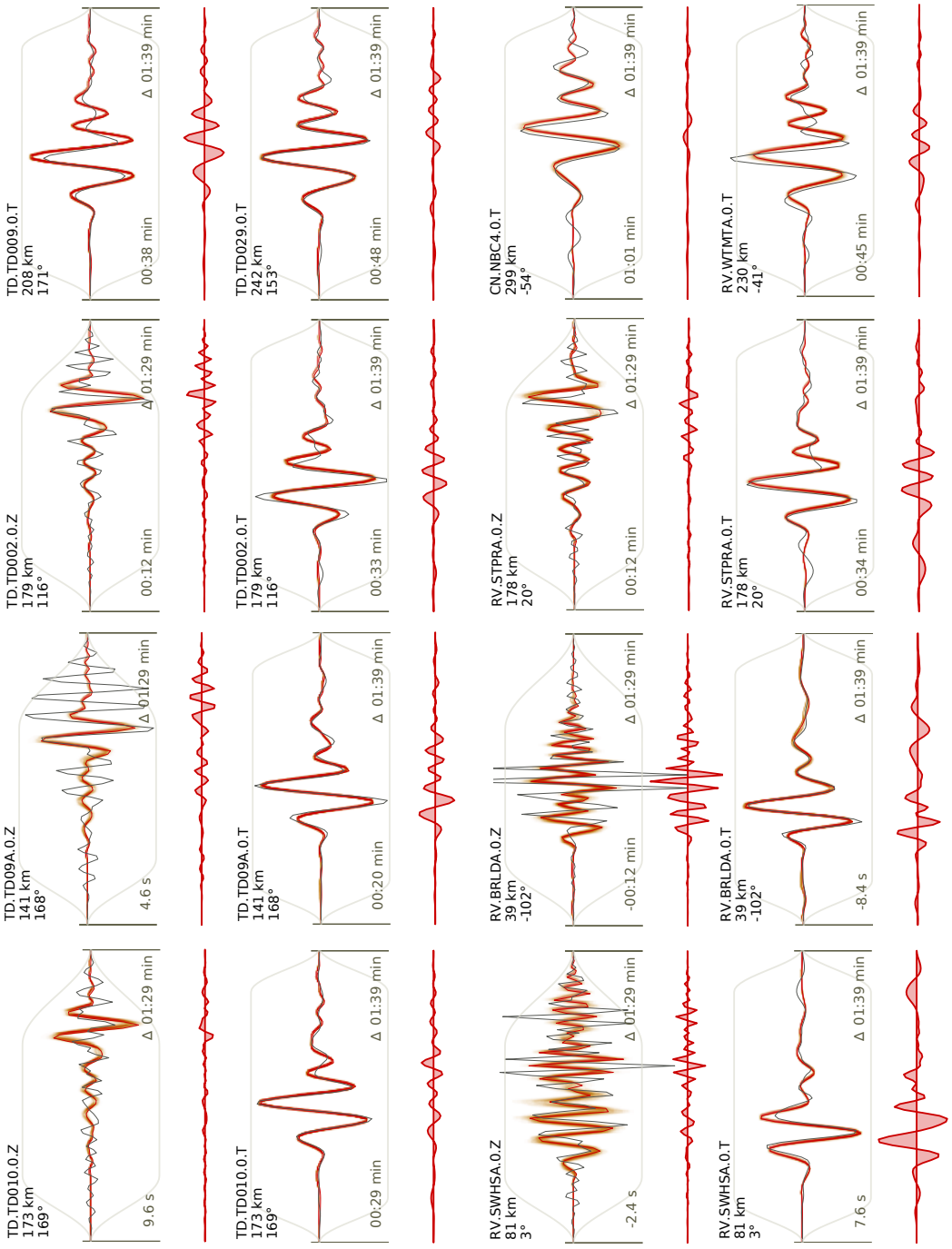

Figure S13. Waveform fits for the full moment tensor solution with *variance* noise parameterisation using the global subsurface structure. A detailed description of plotted features is given in Fig. S12

.

APPENDIX A: SAMPLING ALGORITHM

Using a Monte Carlo method allows drawing samples from a posterior PDF (eq. 1); once enough samples are drawn the resulting distribution is a valid approximation of the posterior probability density (PPD). To sample the posterior PDF we use a Sequential Monte Carlo (SMC) sampler (Moral et al. 2006; Ching & Chen 2007), similar to Minson et al. (2013). Here, we outline the main features of the algorithm, however, for more details we refer the reader to the original references. Obtaining samples from a posterior PDF that has a complex topology (high-dimensional, multimodal, flat, ...) is difficult and inefficient. Therefore, sampling is done starting from the prior PDF via several intermediate PDFs that change following a self adjusting cooling parameter starting at zero (similar to Simulated Annealing (Sambridge & Mosegaard 2002)) (Moral et al. 2006; Minson et al. 2013):

$$\begin{gathered} f(\mathbf{m}|\mathbf{d}_{obs}, \beta_k) \propto p(\mathbf{d}_{obs}|\mathbf{m})^{\beta_k} p(\mathbf{m}) \\ k = 0, 1, ..., K \\ 0 = \beta_0 < \beta_1 < ... < \beta_K = 1 \end{gathered} \tag{A.1}$$

Each intermediate PDF $f(\mathbf{m}|\mathbf{d}_{obs}, \beta_k)$ is sampled in parallel by a pre-defined number of Monte Carlo (MC) chains. Each chain samples the solution space with a predefined number of steps, where step size and directions are determined according to a proposal distribution. When sampling of all chains for the intermediate PDF is completed the algorithm enters a transitional stage:

(i) The likelihood of each Markov chain end-point is used to form an intermediate likelihood distribution.

(ii) This likelihood distribution (at β_k) is compared to the previous intermediate likelihood distribution (at β_{k-1}) by evaluating the coefficient of variation (COV). If they differ significantly (COV > 1) the cooling parameter β_k is incremented only by a small amount. On the other hand, if the distributions are similar (COV < 1) the tempering parameter β_k is increasing faster.

(iii) The proposal distribution is updated based on the distribution of model parameters in the MC chain end-points.

568 (iv) Optional: update $\mathbf{C}$ in each transitional stage using the mean of each model parameter
569 distribution (Dettmer et al. 2007; Minson et al. 2013; Duputel et al. 2014) (see eq. 3).
570 (v) The ensemble of Markov chain end-points at β_{k-1} is resampled according to the inter-
571 mediate likelihoods. Hence, the next stage of Markov chains at β_k are seeded on the end-points
572 of the previous chains, which had the highest likelihoods; unlikely chains are discarded.

573 Finally, if the cooling parameter satisfies $\beta_k \geq 1$, the posterior distribution is reached
574 $f(\mathbf{m}|\mathbf{d}_{obs}, \beta_K = 1) \propto p(\mathbf{m}|\mathbf{d}_{obs})$ and one last sampling of all MC chains with the defined
575 number of steps is executed; then the algorithm stops. For the proposal distribution we use a
576 multivariate Gaussian distribution similarly to Minson et al. (2013).
577